

1992

Formation and desorption of negative ions from metal surfaces

Douglas Hugh Baker

College of William & Mary - Arts & Sciences

Follow this and additional works at: <https://scholarworks.wm.edu/etd>



Part of the [Atomic, Molecular and Optical Physics Commons](#)

Recommended Citation

Baker, Douglas Hugh, "Formation and desorption of negative ions from metal surfaces" (1992).

Dissertations, Theses, and Masters Projects. Paper 1539623825.

<https://dx.doi.org/doi:10.21220/s2-qdsr-6962>

This Dissertation is brought to you for free and open access by the Theses, Dissertations, & Master Projects at W&M ScholarWorks. It has been accepted for inclusion in Dissertations, Theses, and Masters Projects by an authorized administrator of W&M ScholarWorks. For more information, please contact scholarworks@wm.edu.

INFORMATION TO USERS

This manuscript has been reproduced from the microfilm master. UMI films the text directly from the original or copy submitted. Thus, some thesis and dissertation copies are in typewriter face, while others may be from any type of computer printer.

The quality of this reproduction is dependent upon the quality of the copy submitted. Broken or indistinct print, colored or poor quality illustrations and photographs, print bleedthrough, substandard margins, and improper alignment can adversely affect reproduction.

In the unlikely event that the author did not send UMI a complete manuscript and there are missing pages, these will be noted. Also, if unauthorized copyright material had to be removed, a note will indicate the deletion.

Oversize materials (e.g., maps, drawings, charts) are reproduced by sectioning the original, beginning at the upper left-hand corner and continuing from left to right in equal sections with small overlaps. Each original is also photographed in one exposure and is included in reduced form at the back of the book.

Photographs included in the original manuscript have been reproduced xerographically in this copy. Higher quality 6" x 9" black and white photographic prints are available for any photographs or illustrations appearing in this copy for an additional charge. Contact UMI directly to order.

U·M·I

University Microfilms International
A Bell & Howell Information Company
300 North Zeeb Road, Ann Arbor, MI 48106-1346 USA
313/761-4700 800/521-0600



Order Number 9817282

Formation and desorption of negative ions from metal surfaces

Baker, Douglas Hugh, Ph.D.

The College of William and Mary, 1992

U·M·I
300 N. Zeeb Rd.
Ann Arbor, MI 48106

Formation and Desorption of Negative
Ions from Metal Surfaces

A Dissertation

Presented to

The Faculty of the Department of Physics
The College of William and Mary in Virginia

In Partial Fulfillment

Of the Requirement for the Degree of
Doctor of Philosophy

by


Douglas H. Baker

1992

APPROVAL SHEET

This dissertation is submitted in partial fulfillment of
the requirements for the degree of

Doctor of Philosophy

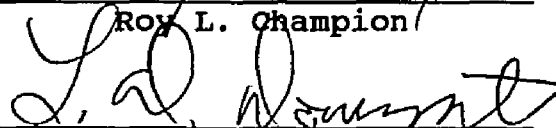


Douglas H. Baker

Approved, September 1992



Roy L. Champion



Lynn D. Doverspike



William J. Kossler



Dennis M. Manos



Stephen K. Knudson,
Department of Chemistry

This dissertation is presented in
honor of Mrs. S.C. Baker and in
loving memory of Hugh and Isa Donnan

TABLE OF CONTENTS

	page
ACKNOWLEDGMENTS	v
LIST OF FIGURES	vii
ABSTRACT	ix
CHAPTER 1. INTRODUCTION	2
CHAPTER 2. ELECTRON AND NEGATIVE EMISSION FROM GAS COVERED SURFACES	10
A. Background	10
B. Experimental Apparatus and Methods	23
C. Results and Discussion	35
D. Summary	67
CHAPTER 3. PHOTON-ASSISTED NEGATIVE ION DESORPTION FROM LOW WORK FUNCTION SURFACES	68
A. Background	68
B. Experimental Apparatus and Methods	75
C. Results and Discussion	81
D. Summary	90
CHAPTER 4. CONCLUSION	91
References	95

ACKNOWLEDGMENTS

I would like to take this opportunity to thank some of the people who have helped me over the last several years:

My advisors Profs. Roy Champion and Lynn Doverspike; I have been extremely fortunate to have been instructed and encouraged by them. They have shown me that above all else, our work is fun.

Dennis Manos, Steve Knudson, and Jack Kossler for reading the manuscript and offering many useful suggestions.

Fred Dylla for his invaluable help in guiding me to useful references and for introducing me to the vacuum big leagues.

Paula Perry, Dianne Fannin, and Sylvia Stout for among other things, registering me, paying me, typing for me and helping me stay out of trouble with the dark side of the bureaucratic forces of evil.

Various mentors I have had during my years here including: Yicheng Wang, Rick Weening, Zhi Wei Lu, and Tim Williams.

My friends, especially those who have helped me: Jim for many useful conversations, AB for listening to practice talks, and Al for assistance with PCs.

Undergraduates who have worked in the lab: Ben Davies, Lee Harrell, John Finn, and Douglas Higinbotham.

Julie, for her companionship, help, and encouragement. She has made the last few years here in Williamsburg very enjoyable.

And finally, my family who have given me much love and support.

List of Figures

Figure	page
1.1 Energy diagram, particle in front of surface . . .	6
2.1 Potential emission mechanism diagram	12
2.2 Apparatus of Winter et al.	15
2.3a Ne ⁺ , Ar ⁺ , Xe ⁺ electron emission	17
2.3b Electron emission statistics	17
2.4 Secondary negative emission coefficients for H ⁻ on various metal surfaces	19
2.5a AES of silicon surface	21
2.5b SIMS of silicon surface	21
2.6 Ion impact apparatus	24
2.7 Parallel plate analyzer	25
2.8 Faraday cup current analysis	27
2.9 Vacuum conditions	32
2.10 Gas handling system	33
2.11 Negative ion yield by Na ⁺ impact	36
2.12 Electron yield by Na ⁺ impact	38
2.13 Total yield by Na ⁺ impact	39
2.14 Negative ion and electron yield by K ⁺ impact . . .	40
2.15 Mass analysis 60 eV by Na ⁺ impact	42
2.16 Mass analysis 100 eV by Na ⁺ impact	43
2.17 Mass analysis 160 eV by Na ⁺ impact	44
2.18 Mass analysis 200 eV by Na ⁺ impact	45
2.19 Mass analysis 250 eV by Na ⁺ impact	46

2.20	Fractional composition of negative ions	47
2.21	Mass analysis 60 eV by K^+ impact	48
2.22	Potential energy diagram O_2^-	51
2.23	Work function change for alkalated Ni	53
2.24	Alkali coverage dependence of negative ion yield .	56
2.25	Alkali coverage dependence of total yield	57
2.26	O^- dependence on alkali coverage	58
2.27	Analysis of dependence on alkali coverage	59
2.28	Collision model	61
2.29	Vacuum conditions during D_2O treatment	64
2.30	Mass analysis after D_2O treatment	65
3.1	Diagram of hydrogen source	73
3.2	Photon impact apparatus	76
3.3	Optical system	78
3.4	Irradiance spectrum of light source	79
3.5	Yield of H^- due to photons	82
3.6	Mass analysis of heated barium	84
3.7	Electron attachment probability	86
3.8	Yield of H^- due to photons	89

ABSTRACT

Investigations of negative ion and electron emission from gas-covered metal surfaces due to the impact of low energy (30 - 300 eV) positive ions and, separately, photons (2 - 5 eV) are presented. In both cases, the negative ion formation process is thought to occur via electron tunneling from the surface or its substrate to a sputtered or photodesorbed neutral atom or molecule.

In particular, absolute total negative ion and electron yields for collisions of positive alkali ions with a gas-covered Mo substrate have been measured. Mass analysis of the sputtered negative ions show that O_2^- is the dominant ion at low impact energies. This coupled with the fact that threshold energies for observing secondary negative ions and electrons are the same suggests that electron production is correlated to the O_2^- production, and specifically that electrons are the result of autodetachment of excited O_2^- . This hypothesis provides an explanation of the mechanism responsible for the emission of electrons at low impact energies.

Relative yields for photodesorbed H^- from a barium substrate have been measured as a function of photon wavelength for the range of 245 to 585 nm. A description of the formation of H^- due to photodesorption of BaH on a surface is consistent with the known energetics of the system. An estimate of the absolute yield of photodesorbed H^- per incident photon has been made.

Formation and Desorption of Negative
Ions from Metal Surfaces

CHAPTER 1
INTRODUCTION

This thesis addresses the topic of negative ion and electron emission from metal surfaces due to the impact of low energy charged particles and photons. The experiments described herein were designed to investigate various mechanisms of negative ion formation and subsequent desorption from such surfaces.

Numerous surface analysis techniques have been developed and implemented in the field of surface science, the majority of which have concentrated on learning about surface structure, composition, bonding (chemisorption and physisorption), diffusion and surface chemistry. Among these techniques, the use of sputtering (removal of a surface's outermost layers by ion bombardment) has become a common first step in preparing a surface for analysis. Sputtering first manifested itself as a metallic deposit on the glass walls of a discharge tube, as first reported by Grove¹ in 1853 and Faraday² in 1854. About half a century later Goldstein³ presented compelling evidence that the metallic deposit was the result of sputtering and was caused by energetic positive ions within the discharge hitting the cathode.

The concept of an individual atomic scale sputtering

event initiated by positive ions was proposed and analyzed extensively by Stark⁴ in 1908. He presented a collision model in which sputtering was viewed as a sequence of binary collision events initiated by one bombarding ion at a time. In this model, the dynamics of elastic collisions were assumed to describe a sputtering event. Stark was also aware of the effect of chemical sputtering, i.e., the formation of volatile compounds by chemical reactions between incident ions and surface atoms.

In a sputtering event, the impact of an incident ion can cause the emission of electrons, ions (positive and negative), neutrals, and photons. The first experiments dealing with the analysis of emitted ions due to sputtering were performed in the late 1930's by Arnot and Milligan⁵, and Sloane and Press⁶. The investigations of Veksler and Ben'iaminovich⁷ and Honig⁸ in the late 1950's marked the beginning of a widening interest in the process of secondary ion emission. Through the mid-1960's a number of other workers added to the expanding bank of knowledge on the general features of secondary ion emission⁹. Of particular relevance to this thesis are the many investigations in the specific area of secondary electron emission by alkali bombardment of gas covered surfaces.¹⁰⁻¹²

Photons have also been used as an analysis probe of surfaces, e.g. the well-known photoelectric effect. In photoelectric studies, electrons which are emitted due to

incident photons are analyzed by determining the number and energy of the emitted electrons as a function of the photon's wavelength. If X-ray photons are used, the technique is called X-ray photoelectron spectroscopy (XPS). This technique is used to determine the electronic structure of solid surfaces as well as to identify surface components chemically. When used in this latter manner, it is sometimes known by the name of electron spectroscopy for chemical analysis (ESCA)¹³. In addition to these techniques, the last few years have seen much activity in the investigation of photon-driven chemical processes. A recent paper by Zhou et al.¹⁴ reviews in depth the topic of photochemistry at adsorbate/metal interfaces.

This thesis is concerned with the collisional dynamics of low energy collisions of positive ions and photons with atoms adsorbed to metallic surfaces. Specifically, this work reports two types of surface experiments, each involving the formation and desorption of negative ions whose neutral parent species were physis- or chemisorbed to the metal surface. The first experiments were designed to investigate the mechanism for emission (or sputtering) of negative ions and, additionally, of secondary electrons due to collisions of low energy positive alkali ions with a gas covered molybdenum surface. Positive ions with energy from 30 eV up to 300 eV were used. The second experiment investigated photo-desorption of negative ions from low work

function surfaces. Photons with wavelengths ranging between visible and near UV were employed in these latter experiments. A barium surface was used in the photo-desorption experiments.

The interesting characteristic that links these two seemingly dissimilar experiments is the idea that the negative ion formation process is due to a common mechanism, namely "electron-tunneling". A model for electron-tunneling has been described in detail by several authors¹⁵⁻¹⁷, and a brief description of this model will follow.

In the electron-tunneling model a neutral atom or molecule is ejected from a metal surface after having adequate energy transferred to it by an incident particle or photon, and, while leaving the surface, charge transfer takes place between the electronic states of the emitted particle and the delocalized states of the valence band of the metal. The electron-tunneling model describes the electronic transition as a resonant electron-transfer process between the unoccupied negative ion states of the emitted neutral particle escaping the surface and the valence band of the metal.

Fig. 1.1 shows the energy diagram for a particle with electron affinity E_a in front of a metal surface with work function ϕ . This affinity energy level E_a shifts and broadens as the particle approaches the surface¹⁸. The energy level shift is due to the attractive interaction

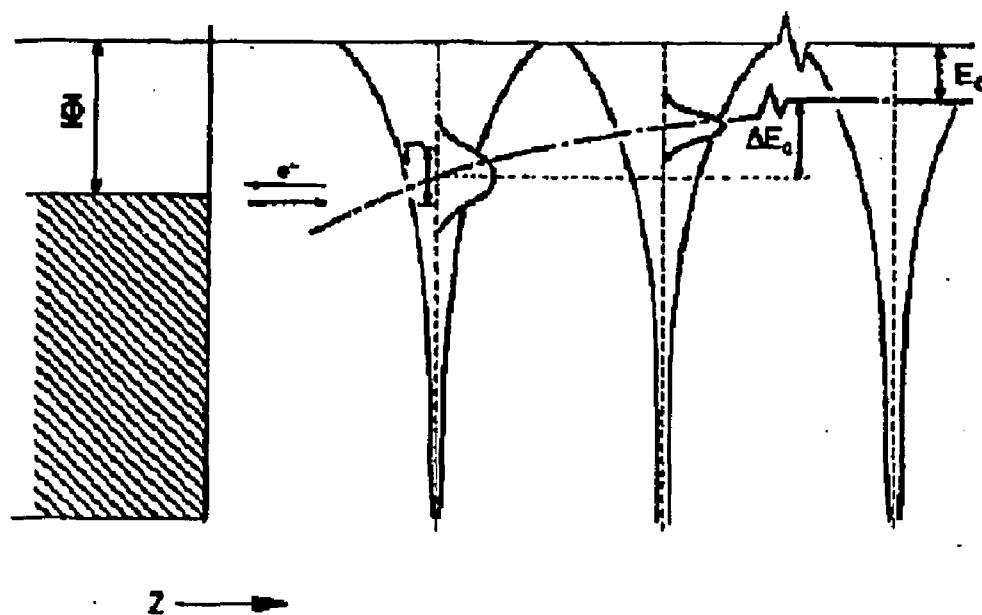


Fig. 1.1. Energy diagram for an atom with electron affinity E_a in front of a metal surface with work function ϕ . The affinity level shifts and broadens as the atom approaches the surface.

between a negative ion and its positive image charge in the metal. This shift, calculated by Gadzuk¹⁹, is given in first order by

$$\Delta E_a(z) = \frac{e^2}{4\pi\epsilon_0} \left[\frac{1}{4(z+k_s^{-1})} \right] \quad (1.1)$$

where e is the electron charge, ϵ_0 is the dielectric permittivity of vacuum, z is the atom-metal distance and k_s^{-1} is the electrostatic screening length in the metal. The screening length k_s^{-1} accounts for the fact that in addition to the interaction between the negative ion and its image charge, there is an interaction between the negative charge distribution in the metal (screening the positive image charge) and the negative ion.

The electron has a finite lifetime in the atomic level and so the energy level broadens in accordance with the uncertainty principle. The width of the energy level $\Gamma(z)$ was described as an exponentially decaying function of z ,

$$\Gamma(z) = \Gamma_0 \exp(-az) \quad (1.2)$$

This z -dependence directly reflects the exponentially decaying electron density in the region outside the metal²⁰.

In experiments discussed herein, an incident energetic particle (or photon) is responsible for the emission of negative ions. It will be suggested that it is the aforementioned shifting and broadening of the affinity level

that will lead to negative ion formation in both types of experiments.

The ion-surface and photon-surface experiments described in this thesis are related to various applications. One such application is the determination of the equilibrium particle concentration in electronic plasmas where energies are comparable to those utilized in these experiments. Another example is the use of Secondary Ion Mass Spectrometry (SIMS), where a more complete understanding of the mechanisms for low energy negative ion emission from surfaces is needed for some systems. For some particle detectors, a complete understanding of secondary emission processes is essential for optimal use and future development of the devices. The present experiments should be relevant for example, to the development of high current negative ion beams for neutral beam injection into tokamaks²¹.

Chapter 2 describes the experiments on electron and negative ion emission from gas covered surfaces due to collisions of incident alkali positive ions. It will be shown that the threshold energies for the sputtering of negative ions and the emission of electrons are identical. It will be suggested that in the near threshold energy region the mechanism for secondary electron-emission involves sputtering an unstable negative ion (formed via electron tunneling) which subsequently decays producing a

free electron.

Chapter 3 describes experiments in which photo-desorption of negative ions from a low work function surface is investigated. Low work function surfaces, in particular barium surfaces, have been used in sources which produce high current negative ion beams²¹. It will be suggested that the analysis and evaluation of these types of negative ion sources should include the role played by photons in the production of negative ions.

A final word about the nature of all of the present experiments described in this thesis is provided as a caveat: The experiments are not like canonical surface-science experiments. Pressures are only kept in the low 10^{-9} Torr range and other than heating, no in situ cleaning or sputtering treatments of surfaces were attempted and no extensive surface analysis techniques were employed. Rather the investigations focused upon developing an understanding of negative ion formation and desorption from gas covered metal surfaces.

CHAPTER 2
ELECTRON AND NEGATIVE ION EMISSION
FROM GAS COVERED SURFACES

A. Background

The experiments described herein investigate the emission of secondary electrons and negative ions due to collisions of positive alkali ions with a gas covered, molybdenum surface. The absolute yields for secondary electrons and negative ions were measured for values of the impact energy ranging from about 30 eV up to 300 eV. The surface's work function could be varied by depositing a fractional layer of alkali metal on the surface. The investigation also included mass analysis of the secondary negative ions.

When a low energy ion or neutral atom hits a surface, emission of electrons, ions (positive and negative), neutrals, and photons occurs. Since the present experiment deals with electron and negative ion emission, it is appropriate to give a brief overview of these two phenomena here.

Secondary electron emission resulting from collisions of positive ions with surfaces has been studied

extensively²²⁻²⁵. Several models for the electron emission process have been proposed, and the conventional descriptions of the origin of the electrons fall into two distinct categories, namely, "potential-" and "kinetic-" emission processes²⁶⁻²⁷.

A potential emission processes may occur when a surface is approached by a low energy positive ion. As the ion approaches the surface, it is neutralized and the neutralization energy (i.e. the difference in energy between the ionization energy of the incident ion and the energy of the neutralizing electron in the metal with respect to the vacuum energy level) can be transmitted to an electron at the surface. The ionization potential of most atoms is greater than the work function of many surfaces. If sufficient energy is transferred to a surface electron in the neutralization process, a surface electron may be emitted from the metal.

Fig. 2.1 shows the energy level diagram of a metal with a positive ion located just outside the metal surface. One electron, referred to as the "down" electron, tunnels through the barrier and drops into the vacant atomic level (E'). The down electron gives up energy $E' - \phi - \zeta_1$, where ϕ is the metal's work function and ζ_1 is an energy level of an electron in the metal. The energy released in this transition is taken up by a second electron, the "up" electron and it gains an energy $E + \phi + \zeta_2$, where E is the

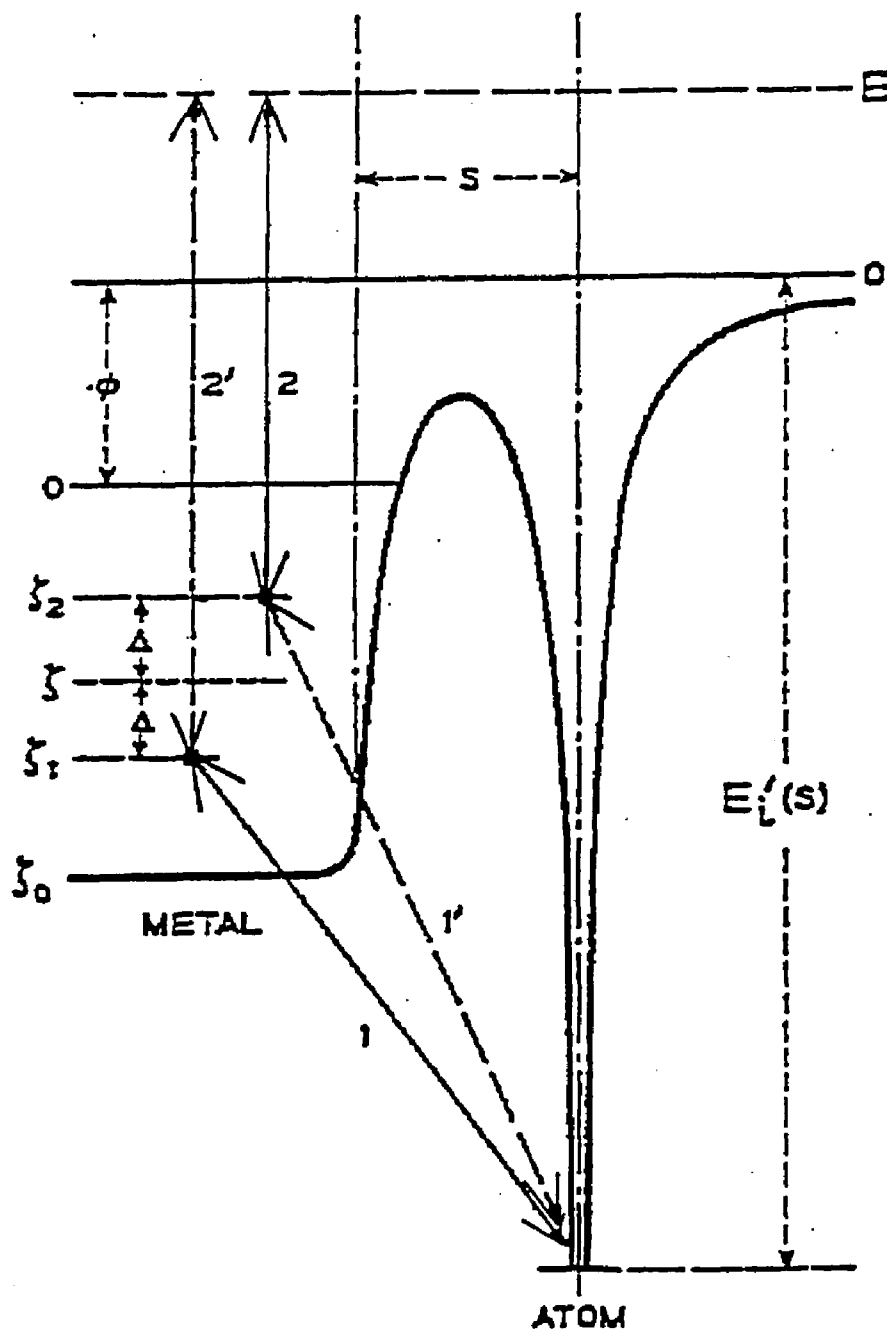


Fig. 2.1. Energy level diagram of a metal with an ion just outside its surface.

electron's kinetic energy and ζ_2 is another energy level in the metal. Equating these two energies gives,

$$E = E' - 2\Phi - \zeta_1 - \zeta_2. \quad (2.1)$$

From this expression it is clear that if the ionization energy (E') of the parent atom of the incident ion is less than twice the work function of the surface, then no electron will be emitted²⁹. In the present experiments, the use of primary positive alkali ions precludes the potential emission mechanism for secondary electrons since the ionization energy of the alkali atom is less than twice the work function of the surface investigated. For example, the work function of molybdenum is around 4.5 eV (an alkali covered molybdenum surface will have a work function no lower than 3 eV), whereas the ionization energy of sodium is 5.1 eV and that of potassium is 4.3 eV.

In the kinetic emission process, momentum is transferred from the incident ion to an electron within the solid. The maximum energy transferred in a head-on collision of an incoming ion with a quasi-free conduction electron is³⁰

$$\Delta E = 2m_e v(v + v_f), \quad (2.2)$$

where v is the ion's velocity and v_f is the electron's Fermi velocity. The results expressed in Eqn. 2.2 are obtained by simply considering an elastic collision between an incident

ion and an electron. Setting $\Delta E = e\phi$, the metallic work function and using reasonable values for $e\phi$ (5 eV) and v_e (10^8 cm/sec), gives a velocity threshold for the kinetic emission of electrons in the vicinity of 10^7 cm/sec (i.e. several hundred eV/amu). Lakits et al.²⁶ point out that this value can only represent an upper limit, because metal valence electrons may exchange momentum with the crystal lattice. This effect can be taken into account by ascribing an "effective mass" to the electron. While this treatment decreases the threshold given by Eqn. 2.2 only slightly, it is found experimentally that for covered surfaces the values for the threshold energies are observed to be significantly lower than thresholds predicted by any of the above models.

Work continues in an effort to extend this simple model and to develop a more detailed understanding of the factors involved in kinetic emission from metals and in particular the mechanism associated with kinetic emission of electrons in the near-threshold region remains an active area of inquiry.

Winter, Aumayr and Lakits²⁷ have made recent advances in the understanding of particle-induced electron emission from surfaces. A schematic diagram of a portion of their apparatus is shown in Fig. 2.2. Primary ions (H^+ , He^+ , Ne^+ , Ar^+ , or Xe^+) are accelerated into the target. The electron detection system is designed such that one can measure the probability of emitting a certain number, n , of electrons.

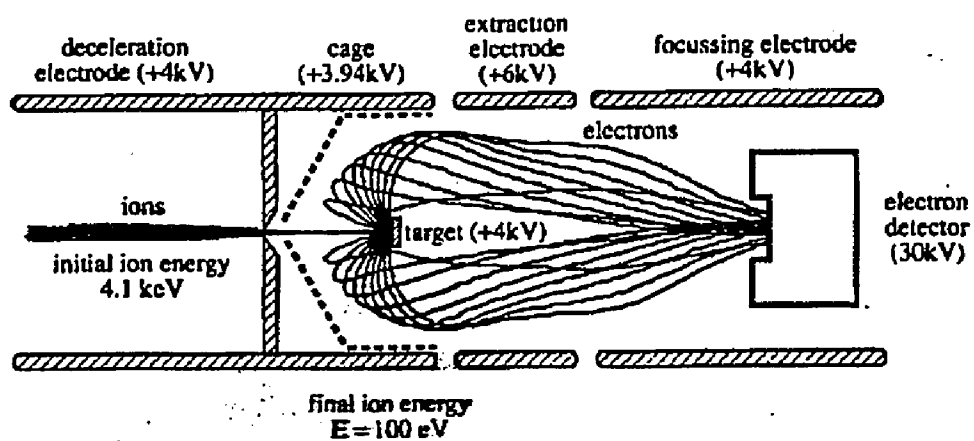


Fig. 2.2. Schematic of Winter et al. experimental setup for measuring particle-induced electron emission statistics and total emission yields for impact of slow ions on a clean gold surface.

The total electron yield, $Y(e^-)$, is defined as the average number of electrons emitted per incident ion,

$$Y(e^-) \equiv \sum_{n=1}^{\infty} nW_n, \quad \sum_{n=0}^{\infty} W_n = 1 \quad (2.3)$$

where W_n is the probability for emission of n electrons per primary ion. They have shown that for the impact of singly charged, ground-state ions the potential-emission mechanism can produce at most, one secondary electron. Therefore by monitoring W_2 and W_1 using the electron detection system illustrated in Fig. 2.2, they can determine precisely the threshold energy for non-potential mechanisms.

Results for Ne^+ , Ar^+ , and Xe^+ impacting a gold surface are shown in Fig. 2.3a where the total electron emission yield is plotted as a function of impact energy per atomic mass unit. In Fig. 2.3b the ratio of emission probabilities W_2/W_1 for emitting, respectively, two and one electrons are plotted as a function of energy per atomic mass unit. The vertical arrows indicate the conventional threshold (i.e. given by Eqn. 2.2) for kinetic electron emission. From these figures it is concluded that a non-potential mechanism is responsible for electron emission for energies below the conventional threshold for kinetic emission. Winter suggests that sputtering of Au excited to autoionizing levels might be responsible for those electrons²⁶. In addition, Winter et al. have pointed out that the absolute

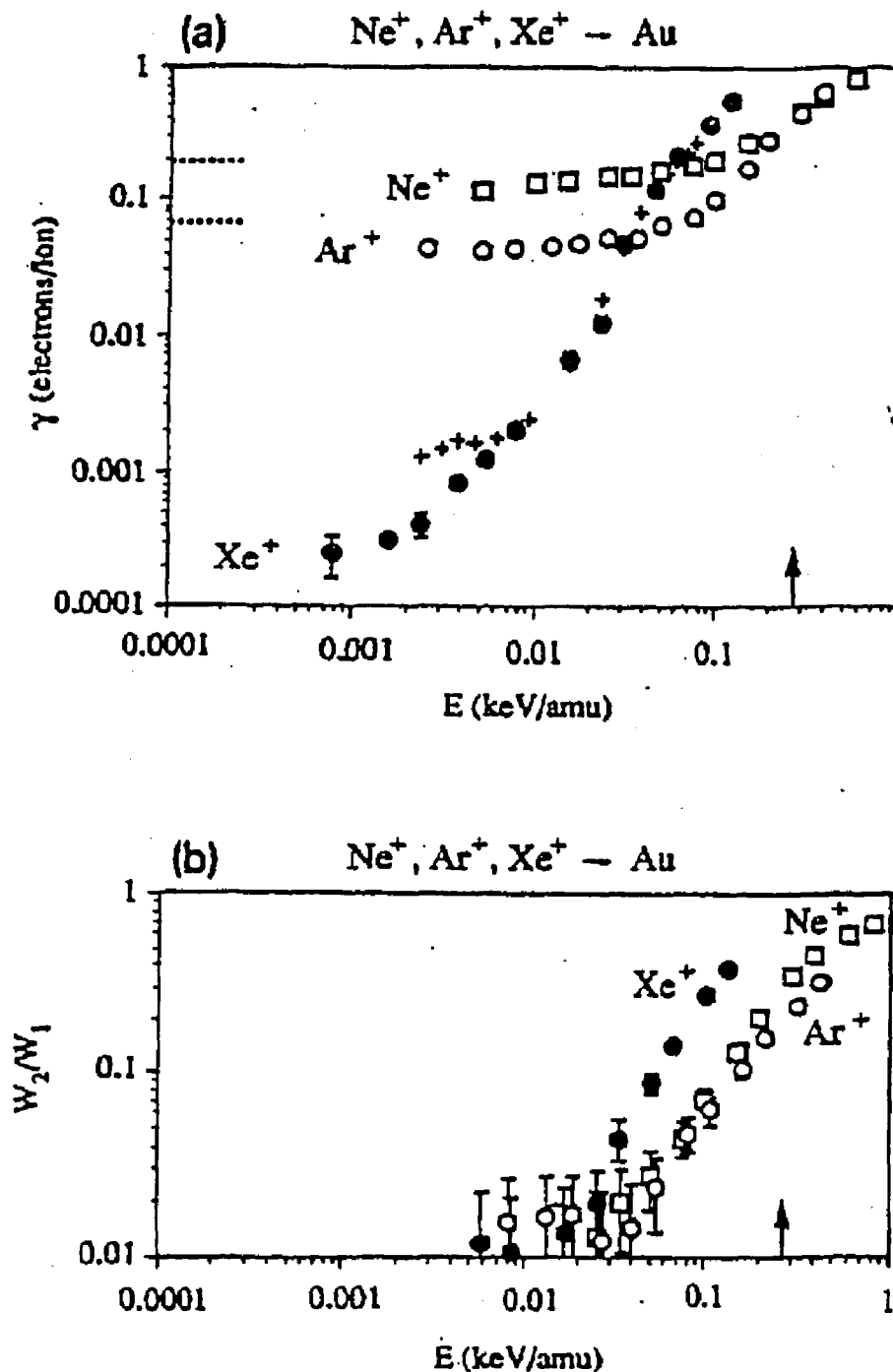


Fig. 2.3. (a) Total electron emission yields for Ne^+ , Ar^+ , and Xe^+ impact on clean polycrystalline gold vs. impact energy per atomic mass unit. The vertical arrow indicates the "conventional" threshold for kinetic electron emission. (b) Ratio of emission probabilities W_2/W_1 for emitting, respectively, two and one electrons for impact of Ne^+ , Ar^+ , and Xe^+ on clean polycrystalline gold vs. impact energy per atomic mass unit

yields (i.e., the measured secondary electron coefficients) in the near-threshold region are very sensitive to surface conditions and have suggested that much of the earlier data for emission coefficients should not be compared to the results of more recent UHV surface experiments in which the surface is clean and well-characterized. Specifically, the kinetic emission of electrons due to collisions of ions (or neutrals) with gas covered surfaces has been observed to be an efficient process for collision velocities considerably below the threshold given above²⁷. Fig. 2.4 shows the secondary negative emission coefficient for H^- on gas covered Cu and stainless steel and on a clean Mo surface as a function of impact energy as measured by Ray et al²⁸.. Comparing the "clean" and the "dirty" surface, it is apparent that the gas layer absorbed on a surface greatly enhances the yield of secondary negative particles. The question now arises as to why these kinds of experiments are so dramatically dependent on surface conditions. Specifically, what is the mechanism responsible for the production of electrons at low collision energies.

Now we address the issue of emission of secondary negative ions from surfaces. A well known use of such emission is found in secondary negative ion mass spectrometry (or more generally SIMS) which was mentioned in Chapter 1. SIMS is a tool used to investigate a surface's composition and/or depth profile. In these experiments, a

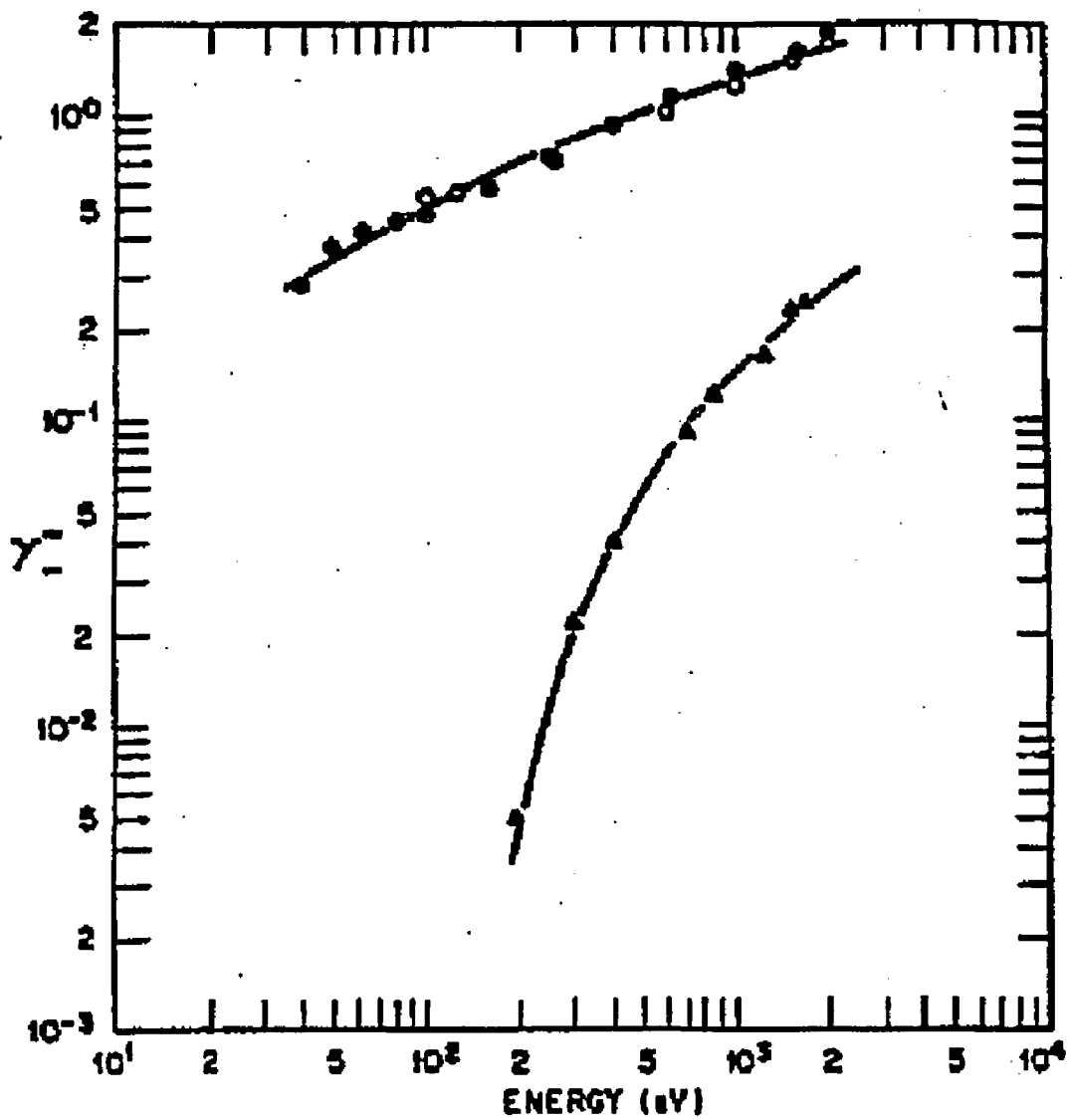


Fig. 2.4. Secondary negative emission coefficient for H^- on gas-covered Cu (●) and gas-covered stainless steel (○) and on a clean Mo surface (▲).

primary beam (typically 5-10 keV positive ions of an inert gas) strikes a surface and the sputtered secondary ions (positive or negative) are then collected and focused into a mass analyzer. A mass spectrum of the secondary ions gives a "fingerprint" of the surface and its contaminants. Fig. 2.5 shows the results of two types of surface analysis techniques of the same silicon surface. Auger electron spectroscopy (AES) consists of bombarding a surface with an electron beam (1 keV or greater in energy) and analyzing the kinetic energy of the secondary electrons. The AES scan in Fig. 2.5a shows signals which can be attributed to an oxide of the sample and small amounts of carbon and calcium. The SIMS scan in Fig. 2.5b however demonstrates the detection of many more trace elements and compounds. The detection of hydrogen which is almost invisible to other surface probes is especially noteworthy. Although SIMS is perhaps the most sensitive surface technique³¹, the mechanism governing the formation and sputtering of negative ions is not well understood for all systems³².

One of the interesting results of the experiments to be presented in this chapter is the suggestion of a possible explanation for the mechanism associated with the production of secondary electrons at low collision energies. This suggested mechanism is somewhat similar to Winter's hypothesis that collisionally-formed autoionizing atoms might be responsible for the secondary electrons which are

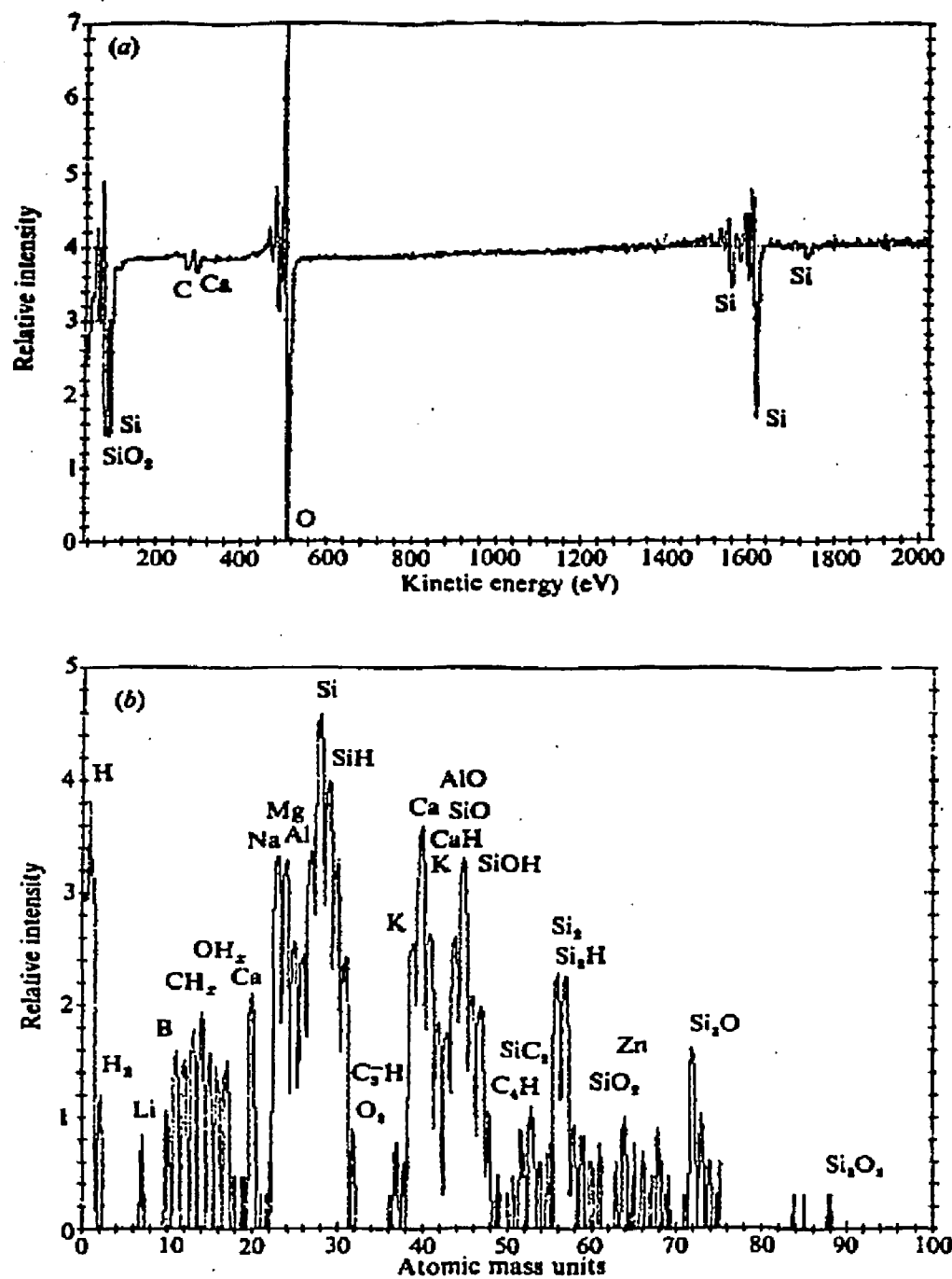


Fig. 2.5. Surface chemical analysis of a Si surface: (a) Auger spectrum; (b) SIMS spectrum.

observed in low energy collisions of ions with surfaces.

Although the surface is undoubtedly gas covered, it is of obvious interest to understand the mechanism(s) for secondary electron emission on such surfaces. As was mentioned earlier, understanding electron and negative ion emission from surfaces due to low energy ion impact is important to a number of areas. In addition to those areas mentioned earlier, the field of plasma-surface interactions would benefit from a comprehensive program to study the impact of low energy particles.³³

B. Experimental Apparatus and Methods

A schematic diagram of the apparatus used in the present experiments is shown in Fig. 2.6. An alkali positive ion beam is extracted from a commercial thermal emission cation source³⁴. The source has a porous tungsten surface which has been impregnated with an alkali compound, and emits a positive alkali beam when heated. The purity of the beam is reported³⁴ to be greater than 99%, with no metastable ions in the beam.

Two lens elements, L_x and L_z , extract the positive ions from the source and focus them into a 45° electrostatic parallel plate analyzer shown in detail in Fig. 2.7.)

The analyzer employs a uniform electric field created by placing a potential difference V across a pair of parallel plates and first order focusing in the deflection plane is obtained when the angle of incidence is 45°³⁵. For transmission, the deflection potential, V is given by $V=2Ed/L$, where d is the plate separation, E is the beam energy and L is the distance between the apertures in the attractor plate ("e" in Fig. 2.6). Satisfying this relationship gives an impact angle (the angle between the surface and the incident trajectory of the positive ions beam) onto the Mo surface of 45°. The same field which focuses the primary beam onto the Mo surface is also employed to extract the negatively charged secondary

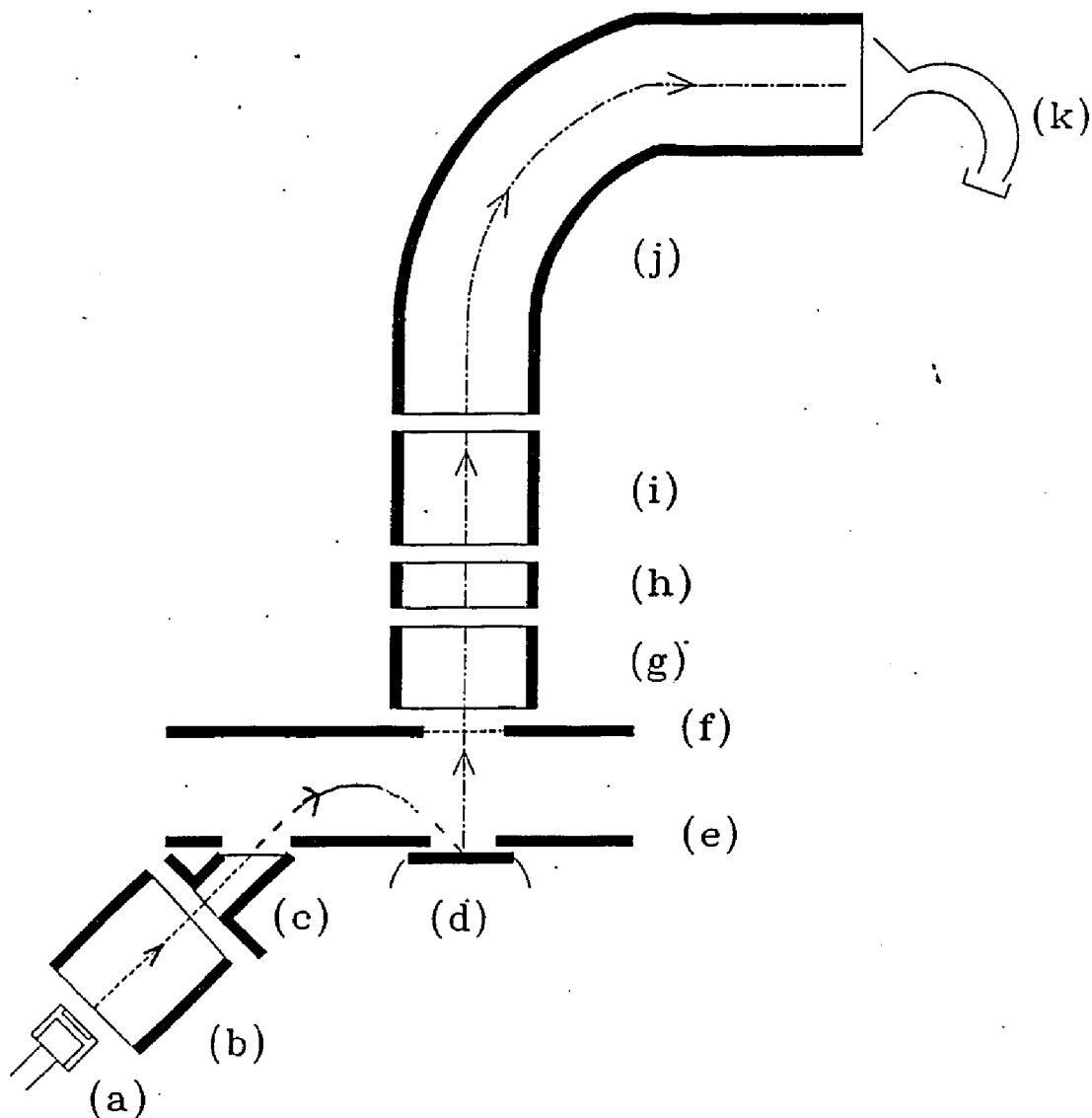


Fig. 2.6. Schematic diagram of experimental apparatus. (a) Ion source; (b) and (c) injection lens; (d) Mo ribbon; (e) and (f) parallel-plate analyzer; (g), (h), and (i) lens; (j) magnetic momentum analyzer; (k) particle detector.

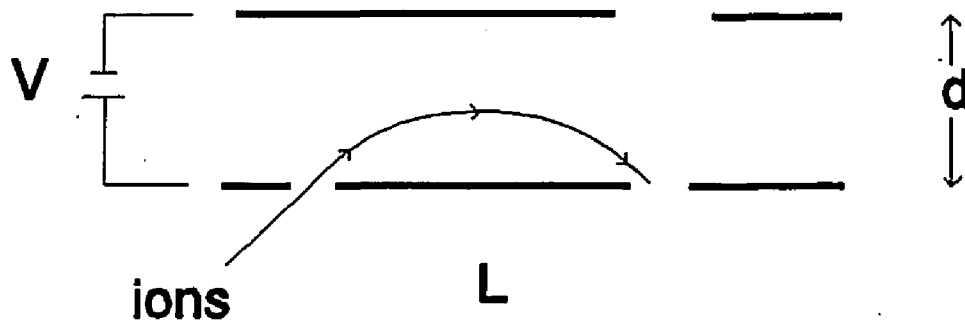


Fig. 2.7. Schematic diagram of parallel plate analyzer.

products from that surface.

The experiment can be operated in one of two modes. In the first, the absolute yield of secondary electrons, and separately, secondary negative ions are measured. In this mode, a Faraday cup replaces the last cylinder on the exit lens stack. An electromagnet, not shown in Fig. 2.6, is located in front of the Faraday cup and can be energized to produce a transverse magnetic field of about 30 Gauss. This field prevents electrons from reaching the Faraday cup while not appreciably affecting the trajectories of the negative ions.

To measure absolute negative ion and electron yields, the incident current to the Mo surface, I_0 , is measured with an electrometer attached to the Mo surface. This current consists of incoming positive alkali ions, outgoing electrons, and outgoing negative ions. Fig. 2.8 demonstrates the effect of the electromagnet's field on the secondary beam. Here the measured current to the Faraday cup, I_s , is plotted as a function of the current applied to the electromagnet. With the electromagnet turned off ($B=0$), a secondary current is measured at the Faraday cup, $I_s(B=0)$, consisting of electrons and negative ions, while at higher magnetic fields, the current to the Faraday cup $I_s(B \neq 0)$ consists solely of negative ions. The negative ion yield, which is defined as the number of secondary negative ions per incident alkali ion, is then:

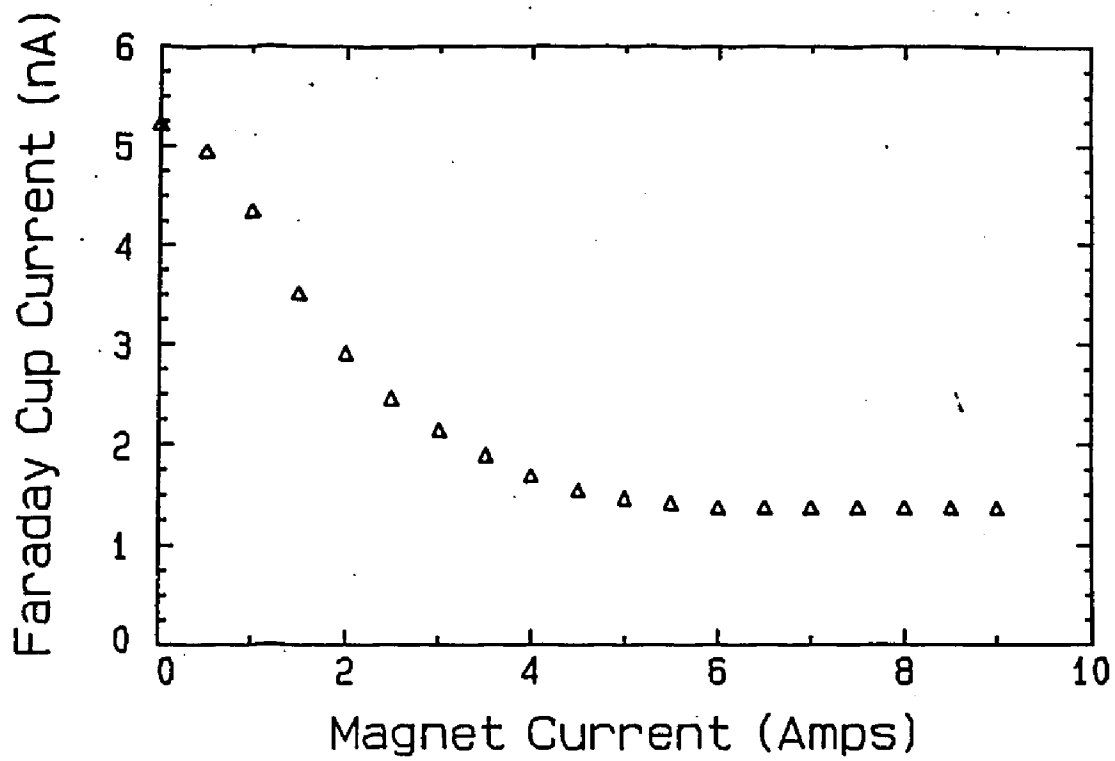


Fig. 2.8. Faraday cup current vs. applied current to the electromagnet.

$$Y(\text{ions}) = \frac{I_s(B \neq 0)}{I_0 - I_s(B=0)}, \quad (2.4)$$

and similarly

$$Y(e^-) = \frac{I_s(B=0) - I_s(B \neq 0)}{I_0 - I_s(B=0)}. \quad (2.5)$$

The aperture in the deflector plate, the Faraday cup, and lens through which the electrons and ions are transmitted are considerably larger than the emitting area of the Mo ribbon. Additionally, the yields, as determined by (2.4) and (2.5), are found to be independent of the lens voltages over a wide range of voltages, leading us to conclude that the absolute transmission factors for detecting ions and electrons are very close to unity.

In the second mode of operating the experiment, the Faraday cup is removed and the ions are focused into a 90° magnetic mass analyzer and subsequently detected by a particle multiplier. The ions pass through the spectrometer tube with a fixed kinetic energy and a mass spectrum is obtained by varying the magnetic field. This mass spectrometer has been used in previous experiments³⁶; these experiments have indicated that its relative transmission factor is independent of mass, within 20%, at least for $1 \leq m \leq 40$ atomic mass units. The particle multiplier used to

detect the negative ions³⁷ has a large aperture and is operated in the pulse mode such that the negative ions strike the input cone of the multiplier with a kinetic energy of 750 eV. At this energy, the detection efficiency is close to unity and independent of mass³⁷. The pulses from the particle multiplier are amplified by an Amptek A-111 charge sensitive amplifier and discriminator. The output pulses from this device are TTL compatible; these TTL pulses can be fed into a scaler so that the secondary negative ion count rate for a particular mass can be monitored.

Mass scans or temporal studies of the secondary ions are obtained through the use of a GPIB data acquisition system. A PC using a National Instruments GPIB controller card is connected to a voltmeter, a scaler and a digital-to-analog programmer. The programmer (Kepco SN 488-122) is used to control the power supply which sets or sweeps the magnetic field in the spectrometer. The voltmeter (Keithley 175) is connected to a gaussmeter and measures the applied magnetic field. The scaler (Aston 721) monitors the count rate from the A-111. The data acquisition system is operated through programs written in Quick Basic.

The Mo sample was cut from technical grade polycrystalline ribbon, 5 mm wide and .020 mm thick. The work function of the ribbon can be lowered by the deposition of alkali atoms from the primary beam. This altered work

function can be controlled by varying the primary beam intensity (typically in the range 0.5 to 5 nA) or the exposure time of the Mo to the primary alkali beam. Typically the sample is heated to a temperature of 1000 K for about 10 minutes before and perhaps during an experiment. This temperature is markedly below the 1800 K needed to rid the surface of molybdenum-oxide³⁸; however the bakeout does remove the absorbed water and any previously deposited alkali metal.

Experiments in the field of surface physics normally require ultra-high vacuum (UHV). Elementary kinetic theory³⁹ provides an estimate of the surface flux, Φ , for a gas at fixed pressure (p) and temperature (T):

$$\Phi = \frac{p}{\sqrt{2\pi mkT}} \quad (2.6)$$

For nitrogen at 300 K and a pressure of 10^{-8} Torr the flux is $5 \times 10^{12}/(\text{cm}^2\text{s})$. If every molecule that strikes the surface sticks, a "clean" surface would be covered with a monolayer of nitrogen in three minutes.

All of the experiments described in this thesis were conducted in a Varian FC12-E Table Top System. This is a metal UHV chamber covered by an elastomer-sealed Pyrex bell jar. The system, pumped by sputter-ion and titanium sublimation pumps, has a base pressure of 2×10^{-9} Torr.

The chamber is initially evacuated by a Sargent-Welch

direct-drive pump. A Zeolite trap in the roughing line prevents backstreaming of hydrocarbon vapors from the roughing pump into the chamber. The trap is baked and cooled before each evacuation is performed. After roughing the chamber to a pressure of 10 microns, the ion pump is started and an all-metal valve is closed with a torque wrench. The entire vacuum chamber is then baked using heater tapes and a Halogen lamp placed inside the vacuum.

The vacuum is monitored in two ways. A standard nude gauge measures total pressure, while an Ametek residual gas analyzer (RGA) gives a rough indication of the partial pressure of various gases in the vacuum. The display of the RGA can be "screen-dumped" to a printer. A sample printout of typical vacuum conditions is shown in Fig. 2.9. Here we see residual gas pressure plotted as a function of atomic mass units. In a leak-free chamber, the dominant partial pressure will be due to water vapor, as is observed here (mass 18). Mass 2 corresponds to hydrogen gas (H_2) and is always prevalent in ion pumped vacuum systems. Also present is nitrogen (N_2), mass 28, and a small peak at mass 43, from the cracking of acetone which is occasionally used as a solvent in cleaning the vacuum components.

Various gases can be injected into the vacuum chamber by using the gas handling system. A schematic of this gas handling system is shown in Fig. 2.10. A Sargent-Welch direct-drive pump has the dual task of first roughing out

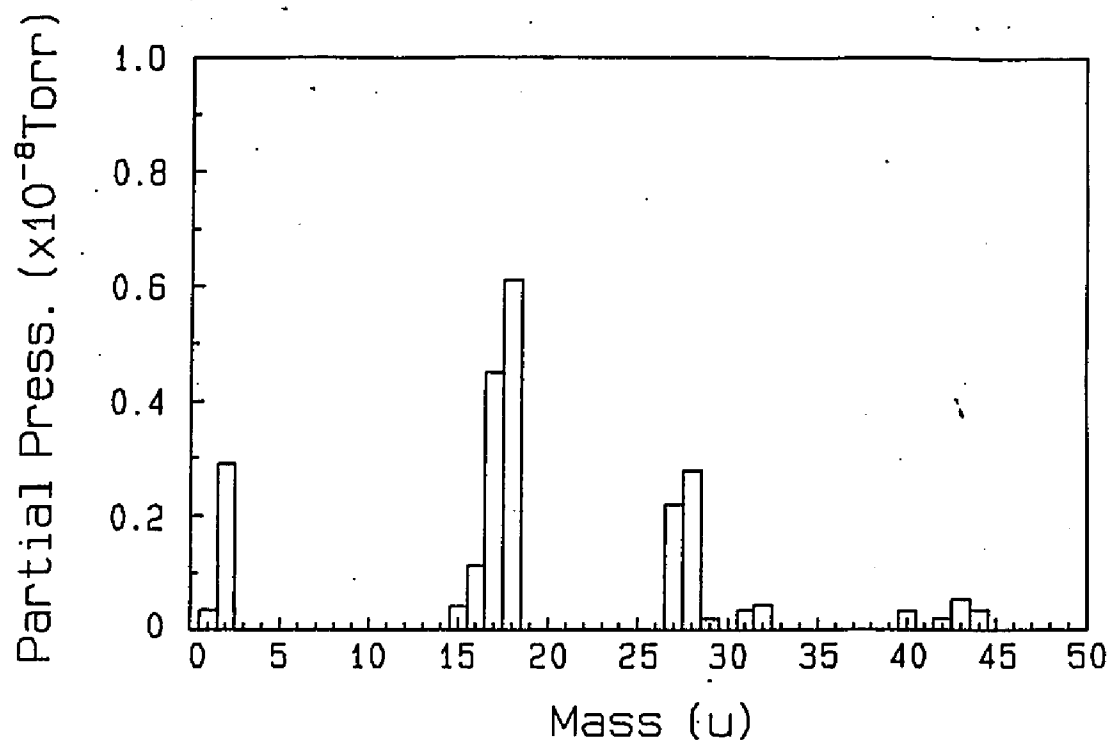


Fig. 2.9. Mass scan taken by residual gas analyzer (Ametek Model # M200) for typical vacuum conditions.

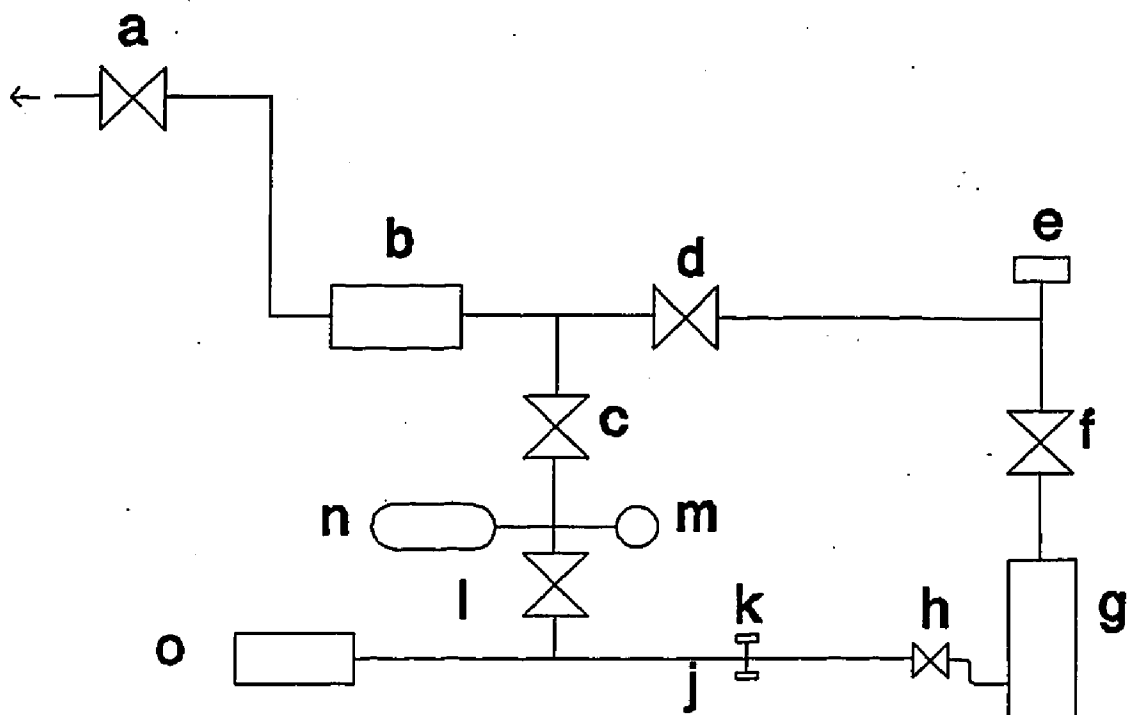


Fig. 2.10. Schematic diagram of gas handling system. (a) leak valve; (b) gas reservoir; (c) and (d) valves; (e) cold cathode gauge; (f) butterfly valve; (g) diffusion pump; (h) and (l) foreline valves; (j) vent; (k) thermocouple pressure gauge; (m) bourdon gauge; (n) lecture bottle; (o) rough pump.

the gas reservoir and vacuum lines above the diffusion pump and also backing the diffusion pump during its operation. A gas is then injected into the reservoir which is then immediately isolated. A Granville Phillips series #203 Variable Leak Valve is then used to control the flow rate of gas into the vacuum with partial pressure resolution of 10^{-10} Torr.

As stated earlier, surface physics experiments require ultra-high vacuum (UHV). To that end, much attention was paid to keeping the vacuum chamber clean, i.e., free of contaminants (such as finger grease) and materials which have high outgassing rates. Electrical connections were made with bare uninsulated wires. Handling of any item to be used in the vacuum was done with latex gloves.

C. Results and Discussion

The absolute yield of negative ions, i.e., the number of secondary negative ions per incident positive ion, is shown in Fig. 2.11 as a function of impact energy for Na^+ hitting the Mo surface at an angle of about 45° . For the results shown in Fig. 2.11, the Mo sample in a vacuum (10^{-9} Torr), was heated to 1000 K for about 10 minutes immediately before the data for curve (a) was collected. Each subsequent curve [(b)-(e)] corresponds to an increased coverage of sodium on the Mo surface. A cubic spline fit is used to generate the solid lines shown in Fig. 2.11 (as well as those in all subsequent plots of yield). Specifically, the Mo sample at 300 K was continuously exposed to an incident Na^+ beam of 5 nA. With this intensity, and the assumption that all ions stick to the surface, approximately 300 minutes are required for establishing a complete monolayer of the alkali metal on the exposed ribbon. The time required for acquiring the data for each curve was under 10 minutes, whereas the exposure time between each of the five runs was about 50 minutes. Thus each curve in Fig. 2.11 is taken with a different fractional coverage by the alkali, but due to the relatively short time required to complete an experimental run, one can assume that the alkali coverage and hence the work function remains approximately constant during each of the five runs.

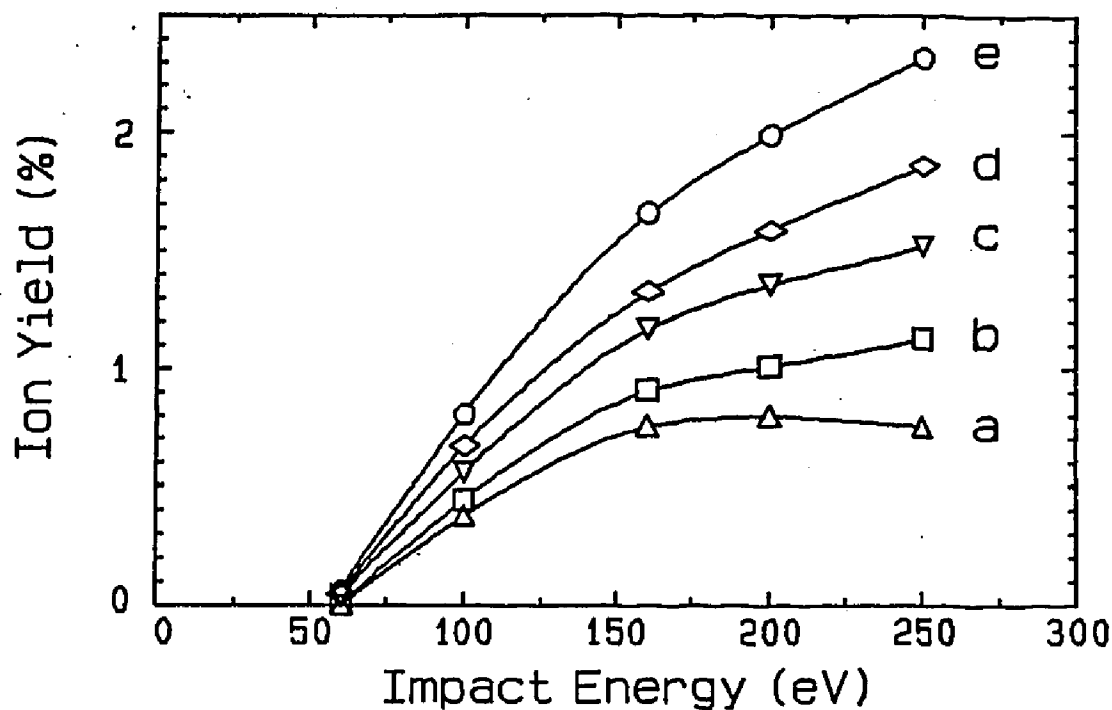


Fig. 2.11. Absolute yield of negative ions for Na^+ projectiles as a function of impact energy. Curves a-e correspond to increasing coverage of alkali metal on the Mo surface: The integrated doses correspond to (a) $0.03S$ ML, (b) $0.2S$ ML, (c) $0.4S$ ML, (d) $0.6S$ ML, (e) $1.0S$ ML, where S is the sticking coefficient for 100-eV Na^+ ions on the surface and where one monolayer (ML) is taken to be $6 \times 10^{14}/\text{cm}^2$.

The ion yields exhibit a clear dependence on the sodium coverage, with increased coverage leading to a higher yield. All curves show distinct thresholds at an impact energy of 60 eV regardless of the amount of alkali coverage. The fifth run, (e), was taken after the Mo surface could have acquired an alkali coverage of about one monolayer, based on the aforementioned assumption that all incident Na^+ sticks.

The yield of electrons as a function of impact energy is shown in Fig. 2.12. The electron yield data [Fig. 2.12 (a)-(e)] were obtained simultaneously with the negative ion yield data [Fig. 2.11 (a)-(e)]. Both negative ion and electron yields exhibit a distinct threshold around 60 eV, and as is true for the ions, the secondary electron yield increases as the alkali coverage of the surface increases. For all coverages the negative ion yields exceed those for secondary electrons for alkali impact energies below 200 eV. The sum of the total yields (electrons and ions) increases almost linearly with energy above the threshold. This is shown in Fig. 2.13 (a) and (e) where the total yield is plotted as a function of the impact energy for two of the curves corresponding to Figs. 2.11 and 2.12 (a) and (e) respectively.

Fig. 2.14 shows both the negative ion and electron yields as a function of impact energy for K^+ hitting the Mo surface for an alkali coverage of about one monolayer. The yields in Fig. 2.14 show similar behavior to their

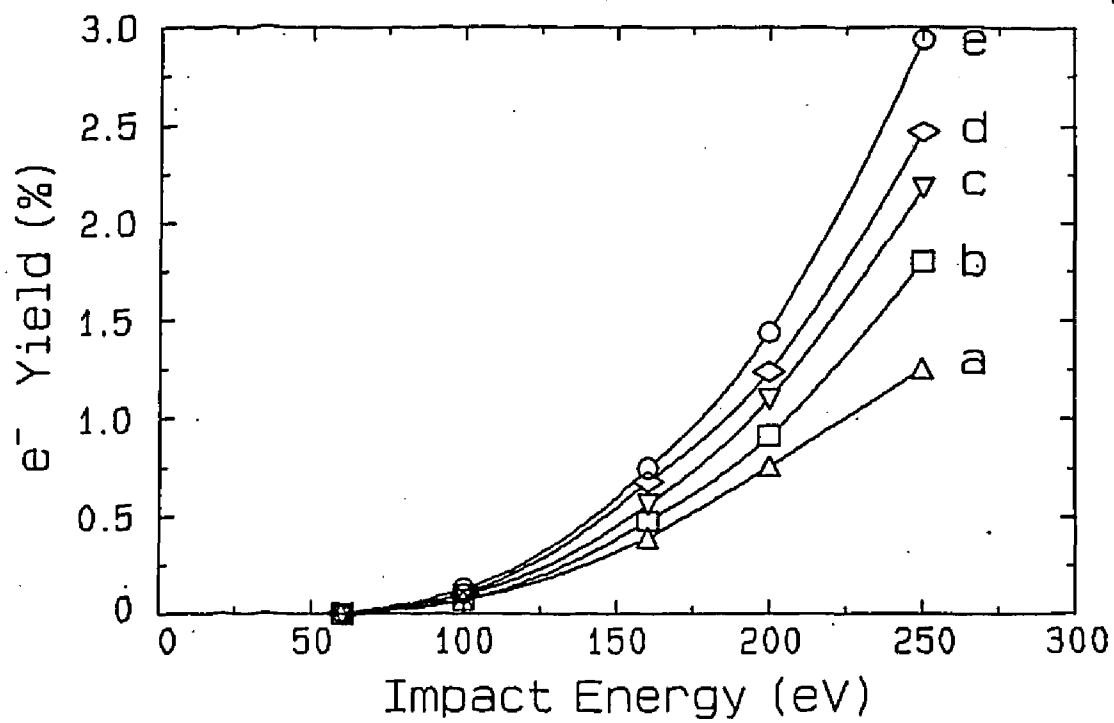


Fig. 2.12. Absolute yield of electrons for Na⁺ projectiles; a-e same as for Fig. 2.11.

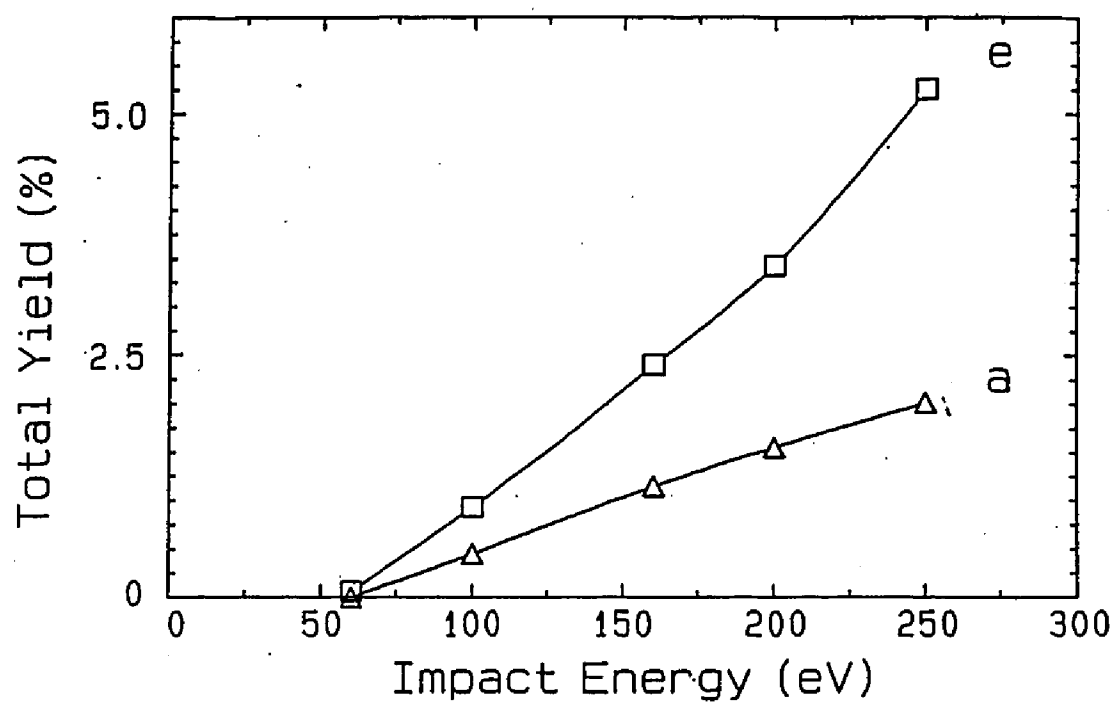


Fig. 2.13. Absolute yield of negative products (negative ions and electrons) for Na^+ projectiles as a function of impact energy. a and e correspond to Fig. 2.11.

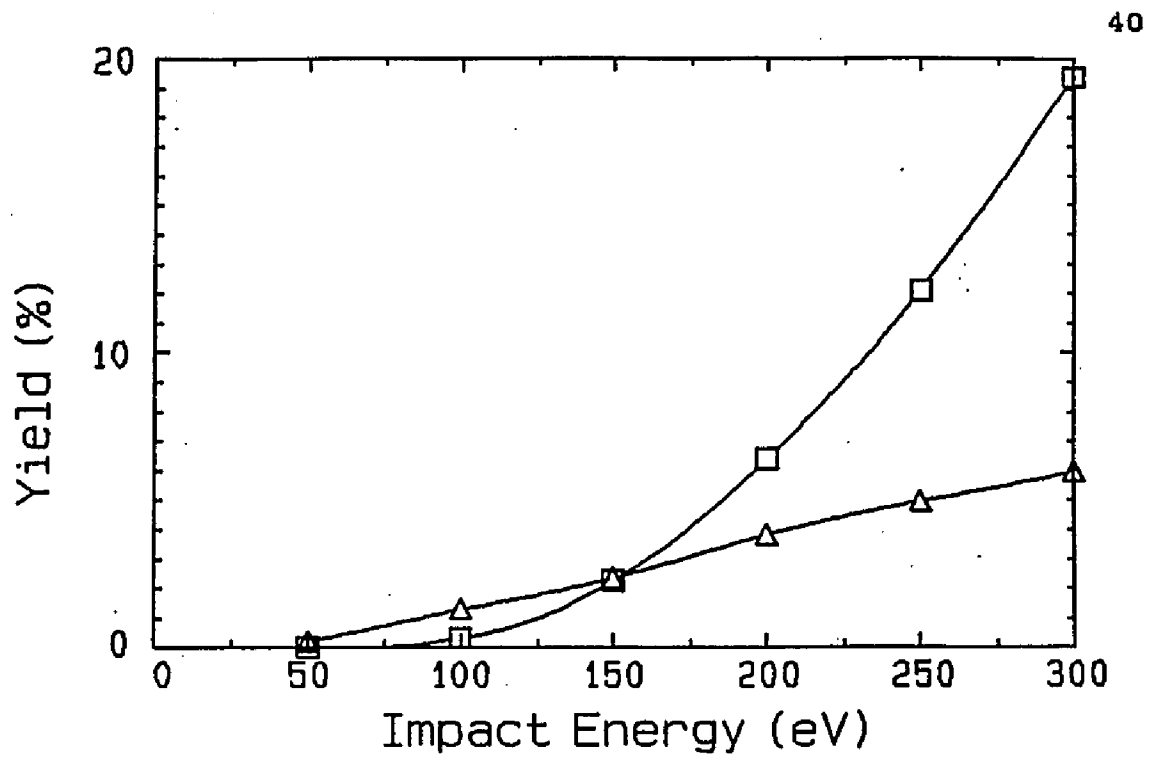


Fig. 2.14 Absolute yield of negative ions(Δ) and of electrons(\square) for K^+ projectiles as a function of impact energy.

corresponding curves in the Na^+ primary beam [i.e. Fig. 2.11(e) and Fig. 2.12(e)]. Fig. 2.14 shows a threshold energy for the production of negative ions around 50 eV. It was found that if one plots the square root of the electron yield as a function of impact energy, the results are approximated by a straight line which extrapolates to a threshold energy for the production of electrons around 70 eV.

Figs. 2.15 through 2.19 show the mass spectra of the sputtered negative ions for the impact energies 60 eV, 100 eV, 160 eV, 200 eV, 250 eV respectively. The molecular negative ion O_2^- is by far the dominant species in the threshold region, while O^- dominates at the higher impact energies. Fig. 2.20 shows the details of the fractional composition of the negative ions taken from the spectra Fig. 2.15 through Fig. 2.19. The four negative ions shown (H^- , C_2^- , O^- , O_2^-) comprise greater than 90% of the total negative ion signal. The remaining negative ions which could be identified in the mass spectra were CH^- and OH^- .

A mass spectrum of sputtered negative ions due to K^+ striking the Mo sample at 60 eV is shown in Fig. 2.21. As is the case for Na^+ striking the Mo at 60 eV (Fig. 2.15), the dominant peak near energy threshold is O_2^- . The similarity of the mass scans and the behavior of the yield measurements for the two projectiles K^+ and Na^+ suggests that these two systems (Na^+ , K^+ striking gas covered Mo) can

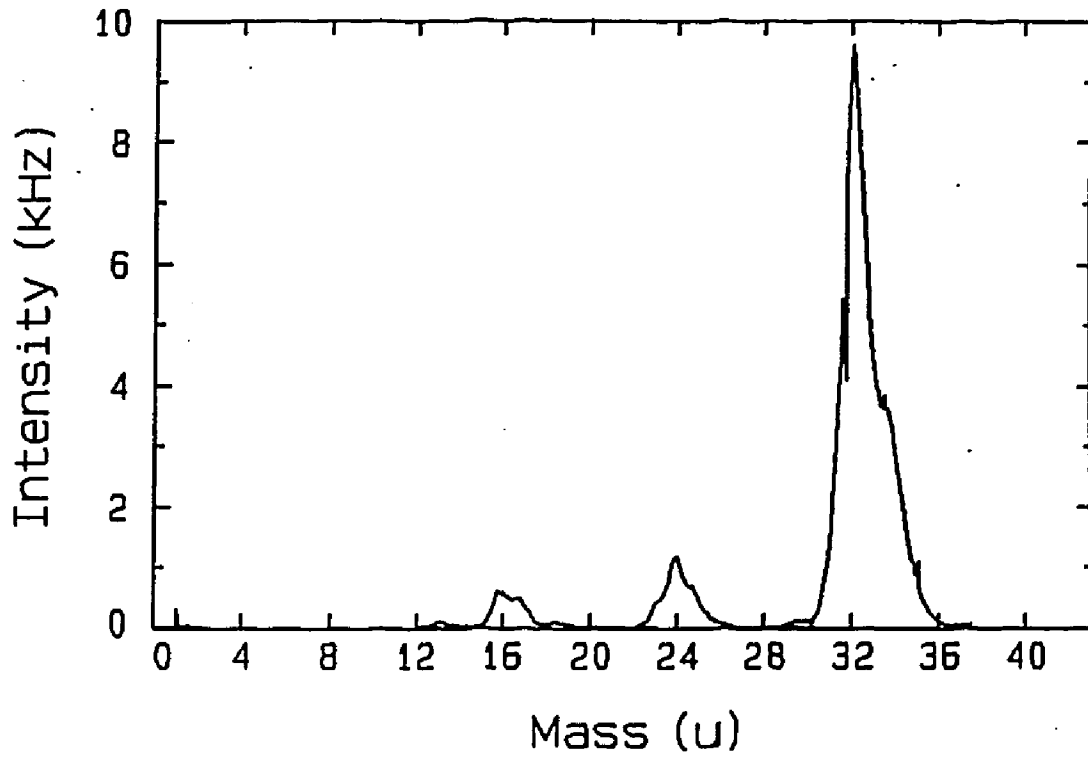


Fig. 2.15. Mass spectrum of negative ions sputtered by 60-eV Na^+ ions impacting Na covered Mo.

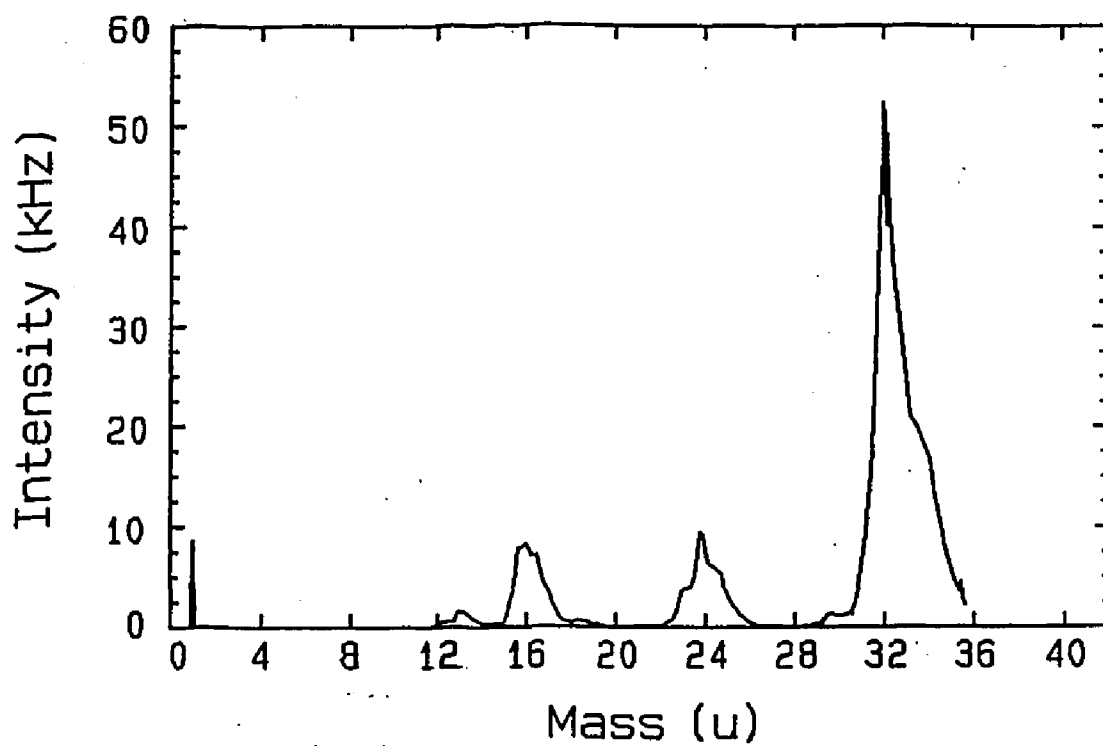


Fig. 2.16. Mass spectrum of negative ions sputtered by 100-eV Na^+ ions impacting Na covered Mo.

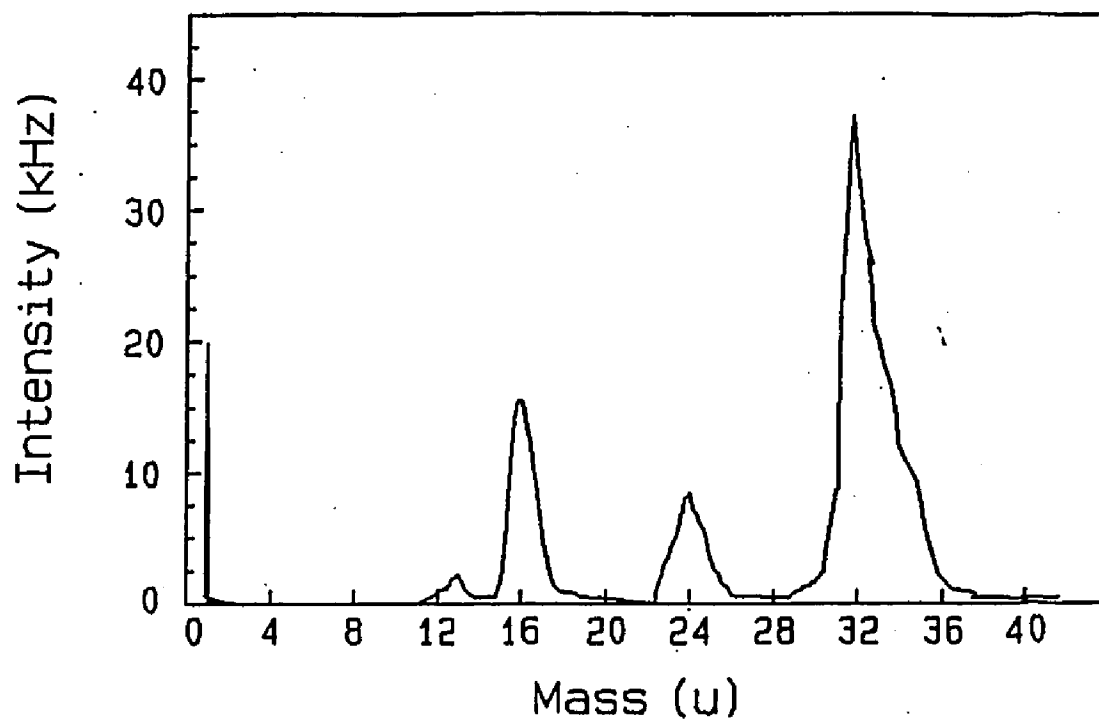


Fig. 2.17 Mass spectrum of negative ions sputtered by 160-eV Na^+ ions impacting Na covered Mo.

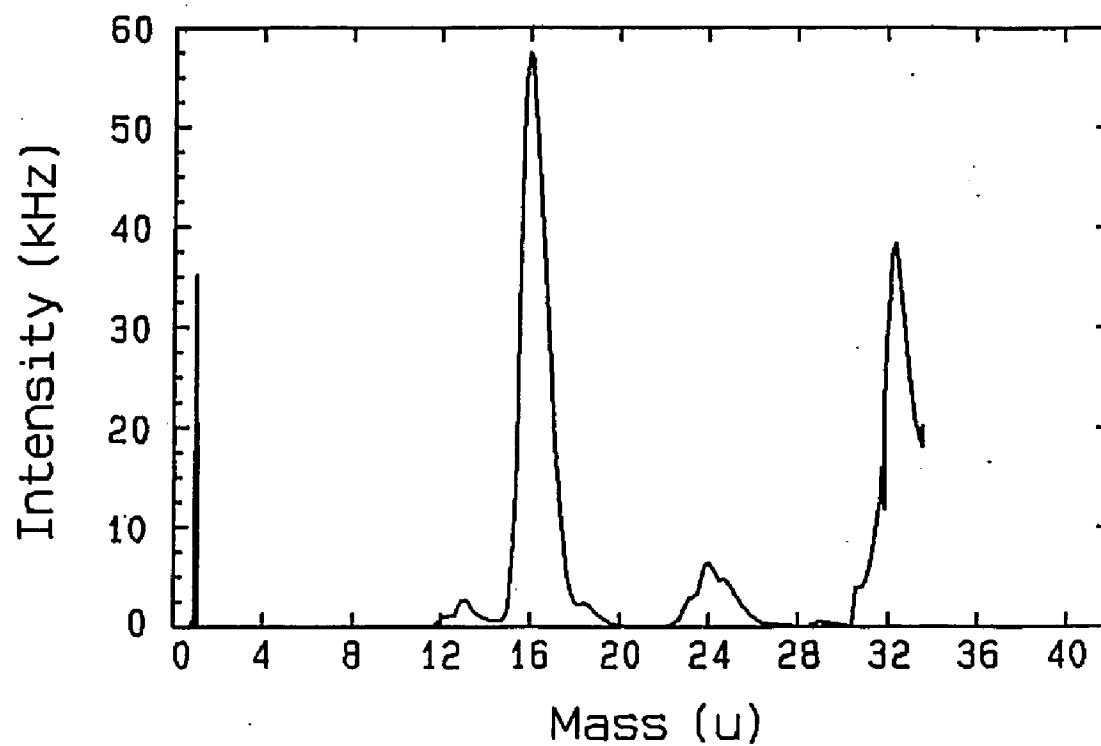


Fig. 2.18 Mass spectrum of negative ions sputtered by 200-eV Na^+ ions impacting Na covered Mo.

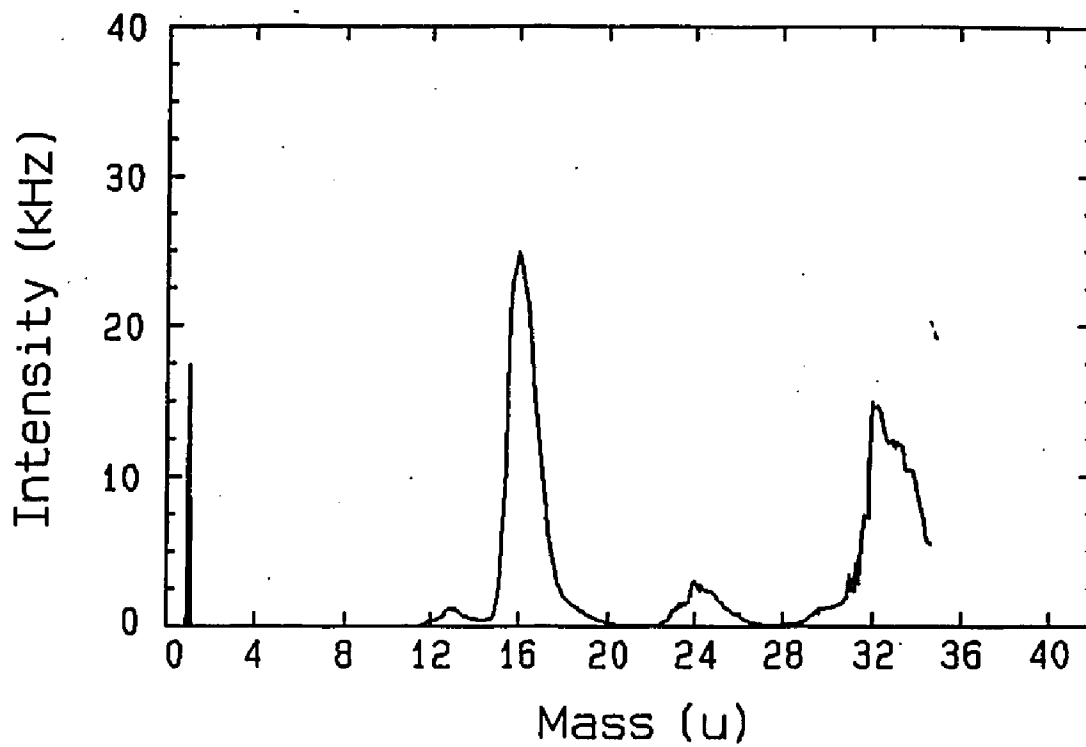


Fig. 2.19. Mass spectrum of negative ions sputtered by 250-eV Na^+ ions impacting Na covered Mo.

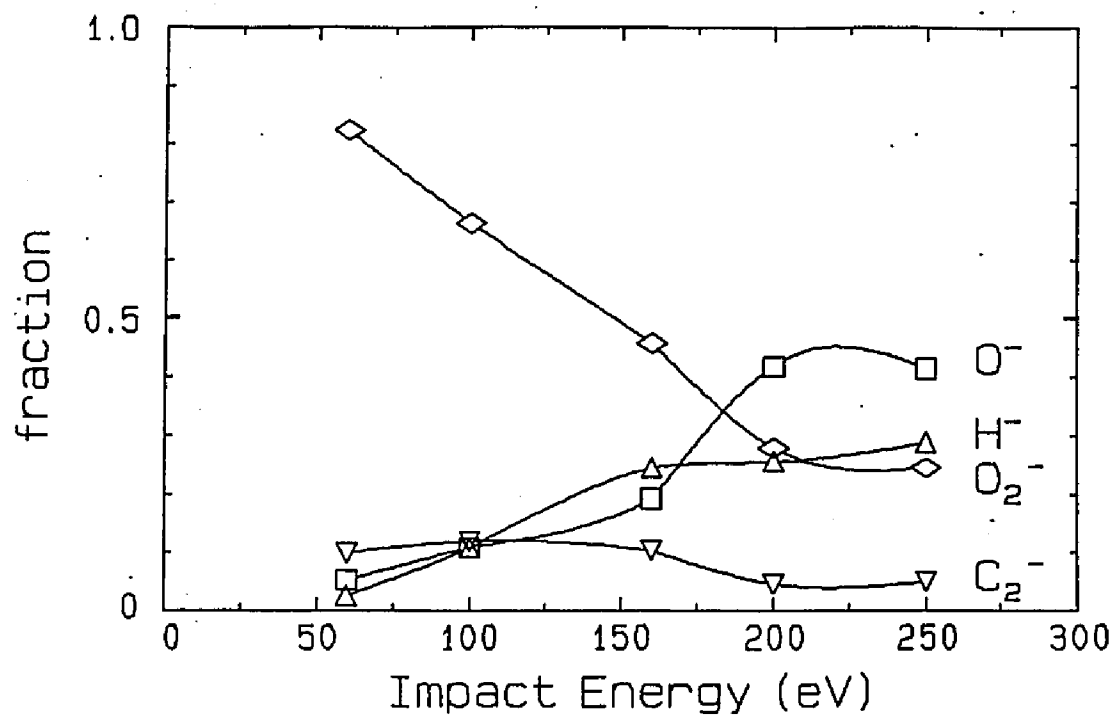


Fig. 2.20. Composition of the negative ions which are sputtered from the surface. \diamond , O_2^- ; Δ , H^- ; \square , O^- ; ∇ , C_2^- . The alkali metal coverage corresponds to the conditions for curve e in Fig. 2.11.

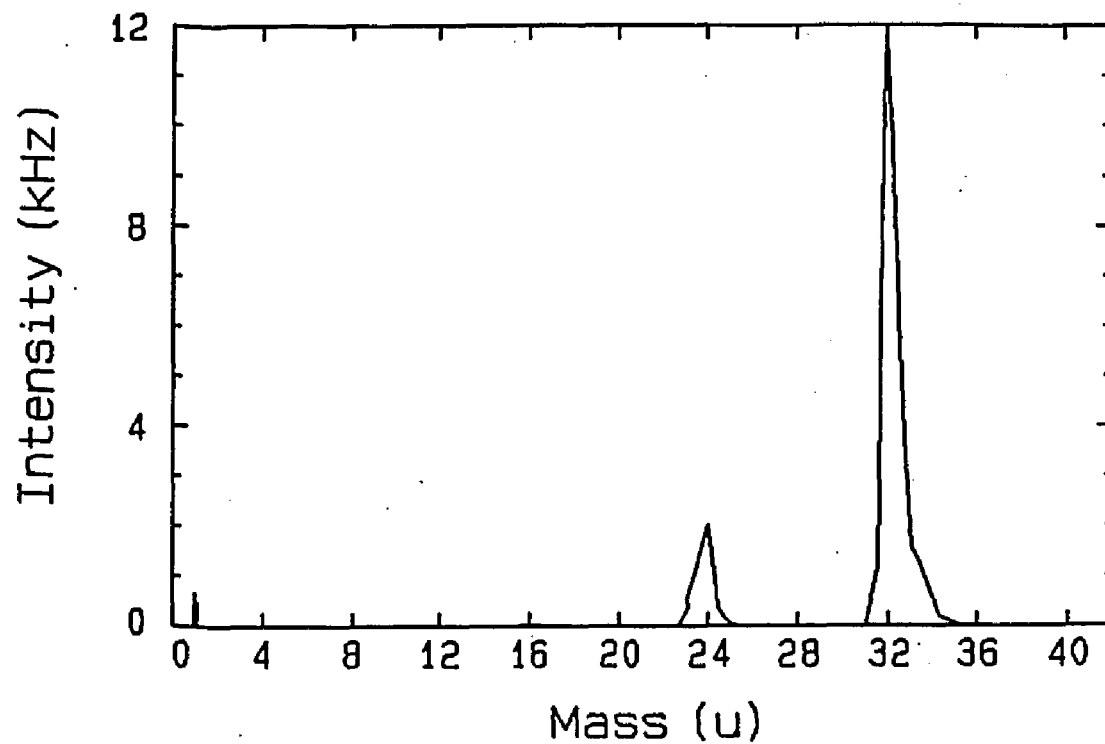


Fig. 2.21. Mass spectrum of negative ions sputtered by 60-eV K^+ ions impacting K covered Mo.

be treated with identical analyses.

Two observations suggest that the electron and negative ion signals originate from a common dynamical mechanism. First, the threshold energies are similar for the electrons and the dominant negative ion species, O_2^- for a given primary beam species. Secondly, both the electron and the negative ion yields at a given impact energy increase in a very similar manner with increased alkali coverage. One possible explanation for these observations is that the incoming positive ion sputters particles, some of which are electronegative and may form both stable and unstable negative ions when leaving the surface. In such a scenario, the unstable negative ions autodesorb giving rise to the secondary electrons observed in the process.

Sputtering of excited atoms is not a novel process in that it has been observed previously. In particular, sputtered excited atoms have been detected by observing the photons emitted during their decay in vacuum.⁴⁰ Tsong and Yusuf⁴¹ have reported absolute photon yields (number of photons emitted at a particular wavelength per sputtered atom) which lie in the range 10^{-2} - 10^{-6} for photon wavelengths of between 200 nm and 800 nm.

For example, $O_2^-(v)$ is unstable if the vibrational quantum number, v , is greater than three. The potential energy diagram of the O_2^- molecular negative ion is shown in Fig. 2.22. It is observed that the O_2^- system is stable

for the lowest three vibrational states in the molecular ion's lowest electronic state. For $v > 3$, O_2^- is metastable and will autodetach into O_2 and a free electron.

In the near-threshold region, we speculate that the average vibrational quantum number, \bar{v} , for $O_2^-(\bar{v})$ is small (below 3) and as the impact energy increases, \bar{v} increases accordingly. Hence at low energy, it would be more likely to observe the stable molecular negative ion, while at higher energies the secondary electron signal would exceed that for O_2^- as is observed in the present experiment. Thus the suggestion is that secondary electron emission for these low energy collisions is not an independent process but rather follows from sputtering an unstable negative ion which autodetaches after the anion is a few angstroms from the surface. Estimating the time it takes an O_2^- molecule with energy around 1 eV (2.4×10^5 cm/s) to travel a few angstroms, gives a value of 1.2×10^{-13} sec. This time is on the same order of the lifetime of the unstable negative ion ($\sim 10^{-14}$ sec).

The formation of sputtered negative ions has been previously treated by the "electron-tunneling model" described in the introduction of this thesis. In this treatment, a neutral is sputtered from a metal by an incident ion, as the neutral leaves the surface, charge transfer can take place between its electronic states and the delocalized states of the valence band of the metal. A

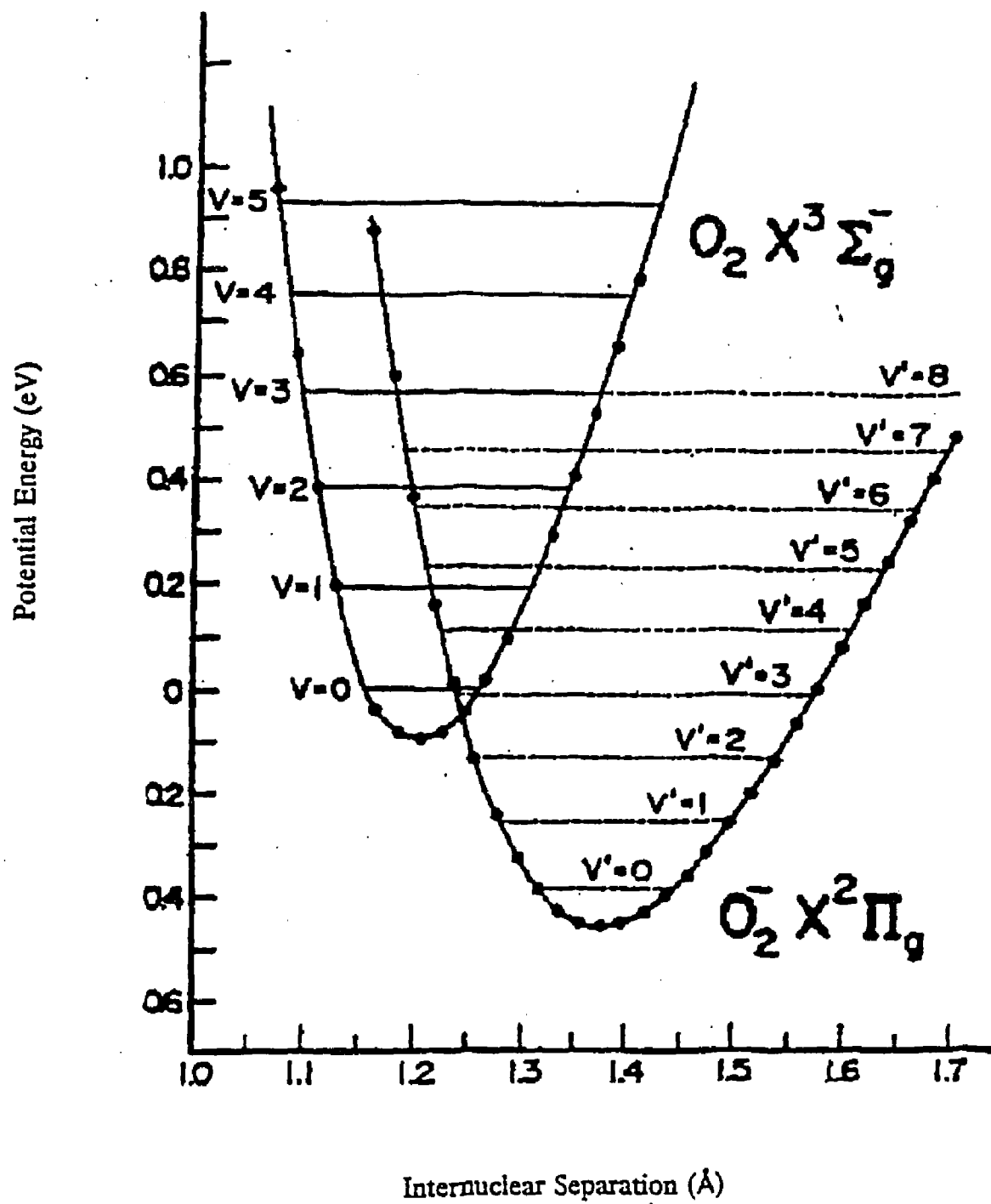


Fig. 2.22. Potential energy curves for O_2^- and O_2 .

salient feature of the electron tunneling model is an exponential dependence of the attachment probability P^- on the work function of the metal:

$$P^- \propto \exp \left[\frac{-(\Phi - A)}{e} \right], \quad (2.7)$$

where Φ is the work function of the surface, A is the electron affinity of the secondary ion, and e is proportional to the perpendicular velocity of the sputtered neutral particle. In other words the faster a newly formed negative ion leaves a surface (i.e. the less time it spends near the surface where charge exchange occurs), the greater the probability that the negative ion will survive.

Fig. 2.23 shows the change in work function $\Delta\Phi$ (eV) plotted as a function of alkali coverage, θ , for Na, K and Cs on Ni⁴². Two features are interesting to point out. First is the approximate linear decrease of Φ with θ for small values of the alkali coverage. Secondly, the minimum of the work function occurs approximately when there is one-half of a complete alkali monolayer. The behavior illustrated in Fig. 2.23 is typical for all alkali metals adsorbed on transition metals⁴². The single valence electron of alkali metals is weakly bound, hence the alkali metals are very electropositive elements, and as solids they exhibit low electron work functions. When adsorbed on a transition metal surface, their valence s-orbital hybridizes with the upper states of the valence band of the substrate

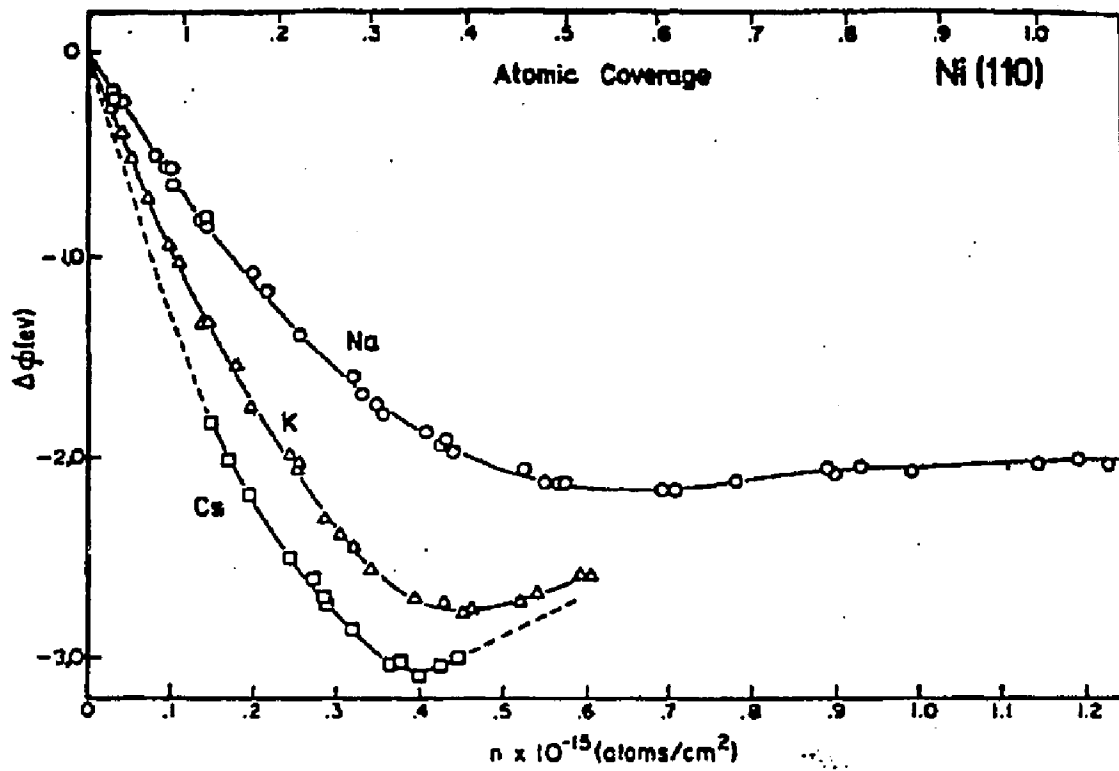


Fig. 2.23. Work function change vs. coverage of Na, K, and Cs on Ni.

metal. The s-state is broadened and lowered in energy, such that it may lose part of its s-electron. As a consequence, the electrostatic potential around the adsorbed alkali species will be lowered, and the alkali species itself becomes partially ionic. Fig. 2.23 demonstrates that the lower the ionization potential of the alkali metal, the larger the dipole moment of the adsorbed alkali metal and the work function change.

This leads us to the question of how the secondary negative ion current i_s changes as a function of alkali coverage, or in other words, for a given primary current, how does i_s change as a function of time. Since $i_s \propto i_p P^-$, Eqn. 2.7 gives $i_s \propto i_p e^{-\Phi/e}$, and then

$$\frac{di_s}{dt} \propto -i_p \left(\frac{d\Phi}{dt} \right) \exp(-\Phi/e), \quad (2.8)$$

From Fig. 2.23 we see that we can approximate $\Phi \approx \Phi_0 - C\theta$ where the coverage $\theta = i_p t$. Hence, $-d\Phi/dt \propto i_p$. Thus Eqn. 2.8 predicts $di_s/dt \propto i_p^\beta$, where $\beta = 2$.

Investigations on the dependency of the negative ion and electron yields on alkali coverage were performed. In most of these experiments, K^+ was employed as a primary beam because of its strong effect on the work function of the sample. In one such experiment, the Mo sample was continuously bombarded with 5 nA of 275 eV K^+ for nearly 7½ hours. During this time the total negative ion yield and electron yields were monitored. The negative ion yields

measured during this experiment are shown in Fig. 2.24. Here it is demonstrated that even with no alkali coverage there is a yield of negative ions and that after 7 hours the ion yield is still increasing.

In a similar experiment, the Mo sample was bombarded with K^+ only when taking total yield measurements. Fig. 2.25 shows total yield of negative products (ions and electrons) as a function of time using 5 nA K^+ . This experiment demonstrates that if the alkali deposition is terminated for any length of time, and then resumed, the electron and negative ion yields also resume unchanged. This result also points out that no appreciable "poisoning" of the surface occurs due to adsorbed gases.

To examine the tunneling mechanism described by Eqn. 2.7, the Mo surface was heated to 1000 K for 10 minutes, cleaning the surface of all previously deposited alkali metal. The Mo surface was then allowed to cool, and the exposure of the surface to the alkali beam was started. The time rate of change in the secondary negative ion signal (di_s/dt) was then measured for various values of the primary current i_p . Fig. 2.26 shows di_s/dt for O^- sputtered from Mo by 160 eV K^+ . Each straight line corresponds to a specific primary beam intensity. The slope, di_s/dt , for each value of i_p was then determined from a linear fitting routine. Fig. 2.27 shows the square root of these values of di_s/dt plotted as a function of i_p . Graphical analysis of the

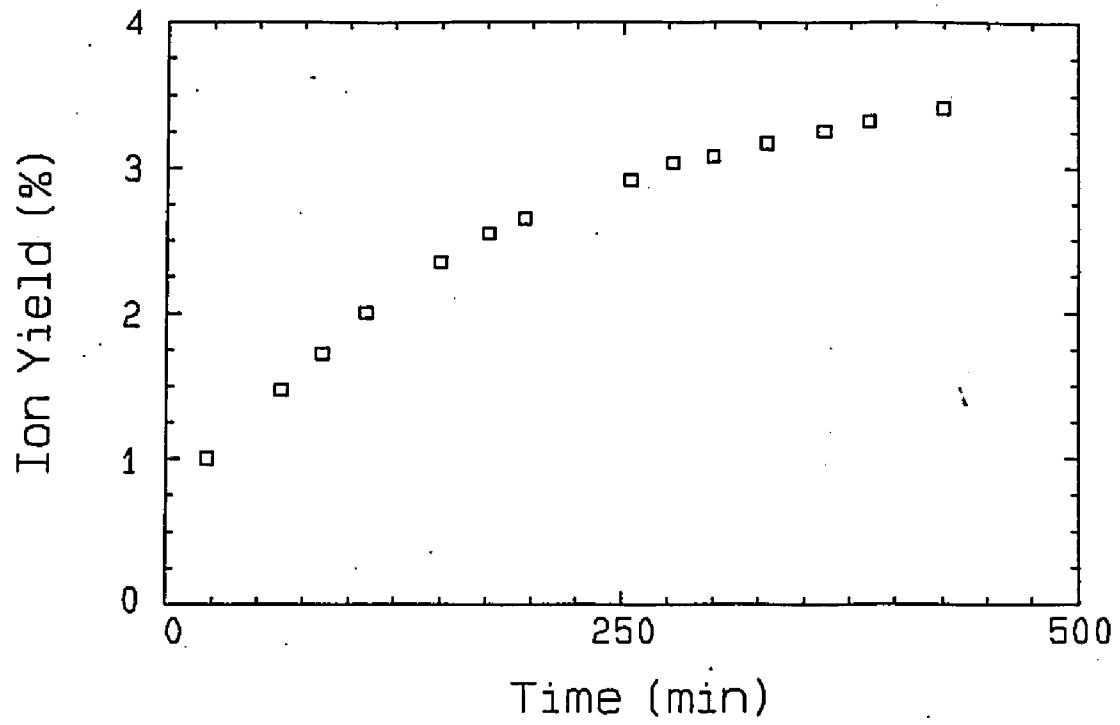


Fig. 2.24. Absolute yield of negative ions for K^+ projectiles as a function of time; constant beam of K^+ .

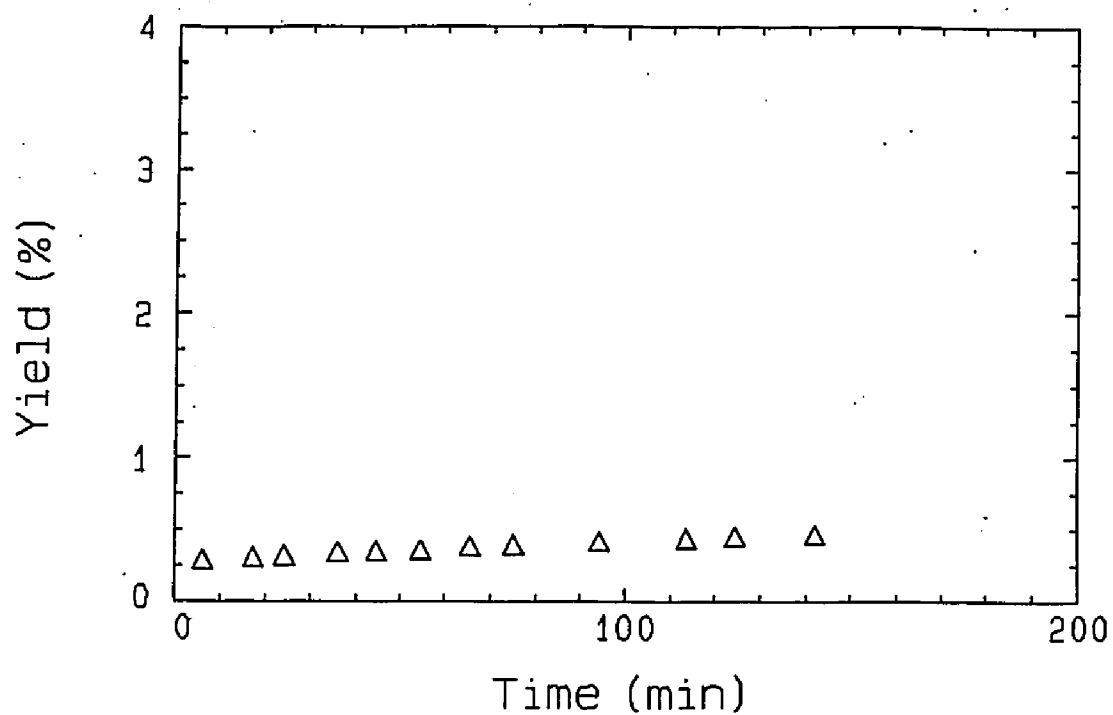


Fig. 2.25. Absolute yield of negative products (negative ions and electrons) for K^+ projectiles as a function of time; the K^+ beam is on only during yield measurement (ordinate same scale as Fig. 2.24 to illustrate the effect of not depositing alkali).

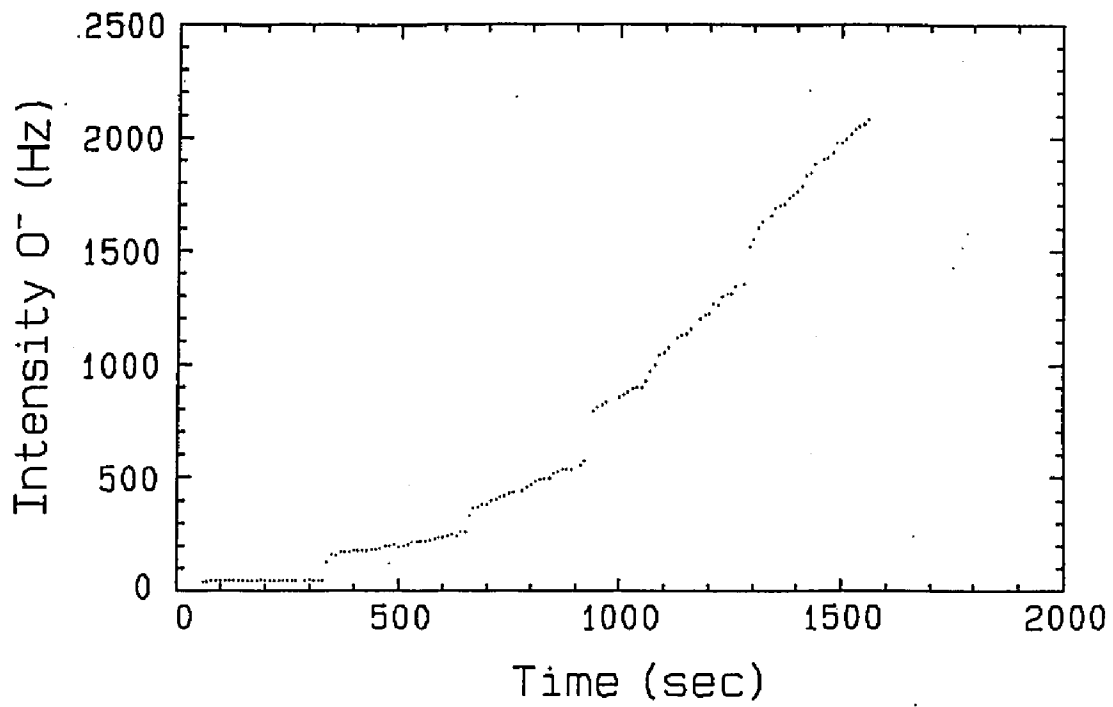


Fig. 2.26. Change in O^- signal as a function of time (di_s/dt) vs. time for K^+ projectiles.

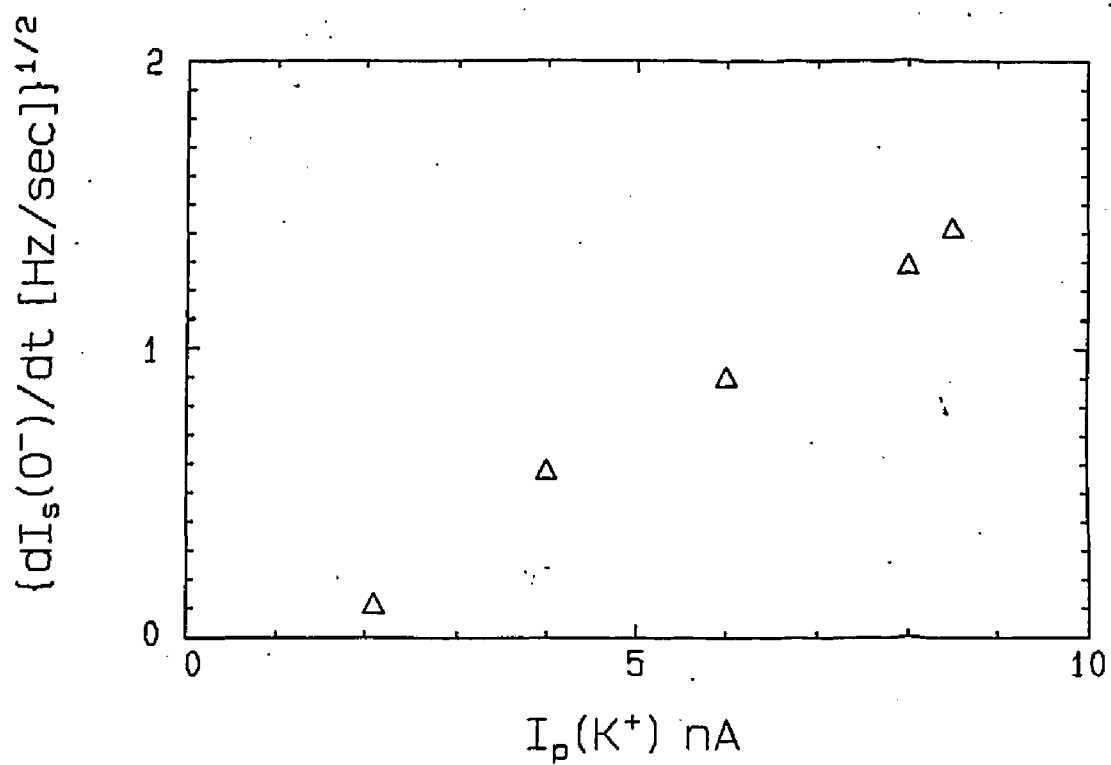


Fig. 2.27. The square root of the slopes from Fig. 2.26 (change in O⁻ intensity as a function of time, d_i/dt) for various values of the primary current (I_p) plotted as a function of I_p .

dependence of di_s/dt on i_p , gives $di_s/dt = i_p^\beta$ where $\beta=2.3\pm 0.3$. This result is in reasonable agreement with the prediction of Eqn. 8.

Now let us turn to the question of the energy thresholds observed in these experiments. In treating sputtering processes, one often makes the simple assumption that the primary projectile of energy E_1 and mass m_1 collides elastically with a surface particle (m_2), losing a fraction, γ_1 , of its original kinetic energy. A second collision can then transfer $\gamma_2(1-\gamma_1)E_1=\Delta E$ to a third particle (m_3). If ΔE exceeds the surface binding energy of the third particle then it may be ejected from the surface. With Na^+ as the primary beam, the energy threshold for O_2^- is observed to be 60 eV, with K^+ the threshold is observed to be 50 eV. It is clear that $\gamma_2(1-\gamma_1)$ must be of order 0.1 as binding energies are typically several eV. Let us take a simple example which is illustrated in Fig. 2.28: if Na^+ collides with a surface particle and is deflected 45° (i.e. scatters into the plane of the surface in the present experiment), then $0 < \gamma_1 < .5$, depending on whether m_2 is M_0 ($\gamma_1=0$) or $m_2=m_1$ ($\gamma_1=0.5$). In a second binary collision with, e.g., O_2 , the oxygen molecule rebounds with an energy $\gamma_1(1-\gamma_2)=(.97\gamma_1\cos^2\theta)$ for the case of Na^+ on O_2 , where θ is the recoil angle of O_2 with respect to that of Na^+ which, in this example, is in the plane of the surface. It is clear that large angles are required for sputtering and for

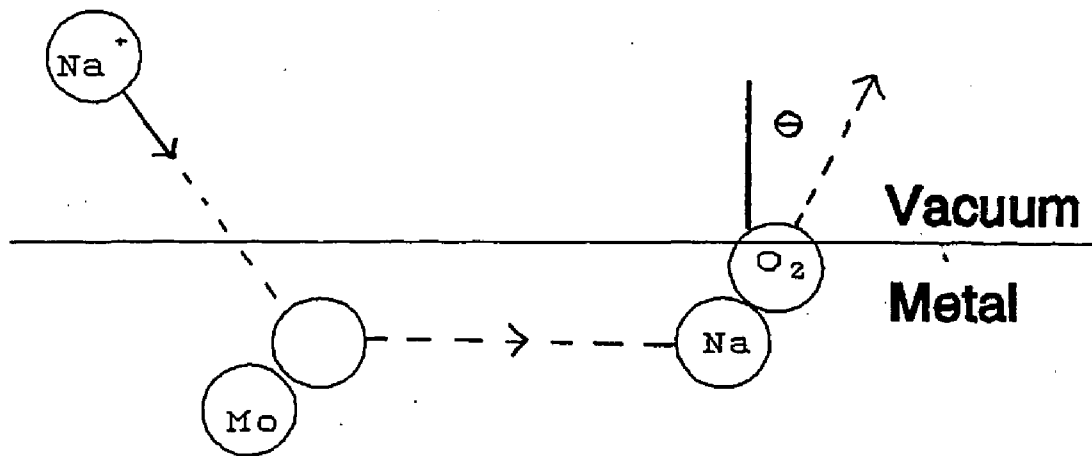


Fig. 2.28. Schematic of ion-surface collision.

simultaneously maximizing the attachment probability P^- of Eqn. 7. [ϵ is proportional to the outgoing projectile's component of velocity normal to the surface⁴³.]

Specifically, if one uses this model to calculate θ for O_2 (assuming E_1 is 60 eV and m_2 is M_o) such that the kinetic energy transferred to the O_2 molecule is greater than 5 eV (typical binding energy), it is found that θ must be less than 17° . In conclusion, it is clear that a simple two-step model such as that described above can yield values of $\gamma_1(1-\gamma_2)\cos^2\theta$ in the neighborhood of 0.1; the data which exhibit thresholds at $E_1=60\text{eV}$ (Na^+) and $E_1=50\text{eV}$ (K^+) are then at least compatible with such a model. A similar argument applied to the sputtering of H^- would predict a higher threshold energy, in accord with our results shown in Fig. 2.20.

Experiments were performed to investigate the sources of the neutral parents of the observed ions were performed. In one series of investigations, the Mo was heated to 1000 K for 10 minutes before each experiment and then subjected to doses of up to 800 Langmuir (1 Langmuir is an exposure of 10^{-6} Torr for 1 sec) of water, a prevalent surface contaminant, by introducing water vapor into the vacuum at partial pressures varying from 10^{-9} to 10^{-7} Torr. It was observed throughout these experiments that neither the total negative ion yield nor the total electron yield was affected by this exposure to H_2O .

In another test, equal partial pressures of H_2O and D_2O were introduced into the vacuum. Fig. 2.29 shows the RGA scan of the background gas during the H_2O/D_2O exposure. After a dose of a few Langmuir only a small D^+ signal shown in Fig. 2.30 (<1% of the H^+) signal was detectable. We are then led to the conclusion that water vapor adsorbed on the surface of the sample due to our dosing is not an important source of the observed desorbed ions.

The source of the H^+ signal is intriguing. As mentioned in the introduction of this chapter, SIMS is best suited for investigating hydrogen in surfaces. Again, the persistence of the H^+ signal even after heating the surface to 1000 K leads one to conclude that sources of hydrogen other than absorbed water or hydrocarbons, such as interstitial hydrogen, are responsible for the H^+ observed. It has been reported by other investigators that a surface with an oxide layer will continue to have H_2 outgassing even after conventional bakeouts⁴⁴ (20 hour bakeout under vacuum at 100° C). The notion is that oxide layers inhibit hydrogen from diffusing across the metal/vacuum interface and desorbing into the vacuum. It follows then that if this idea is correct and one wants to remove the hydrogen from Mo, the sample must be baked to at least 1800 K so as to remove the oxide layer first.

Additional experiments conducted by subjecting the surface to doses of H_2 resulted in no change in the H^+

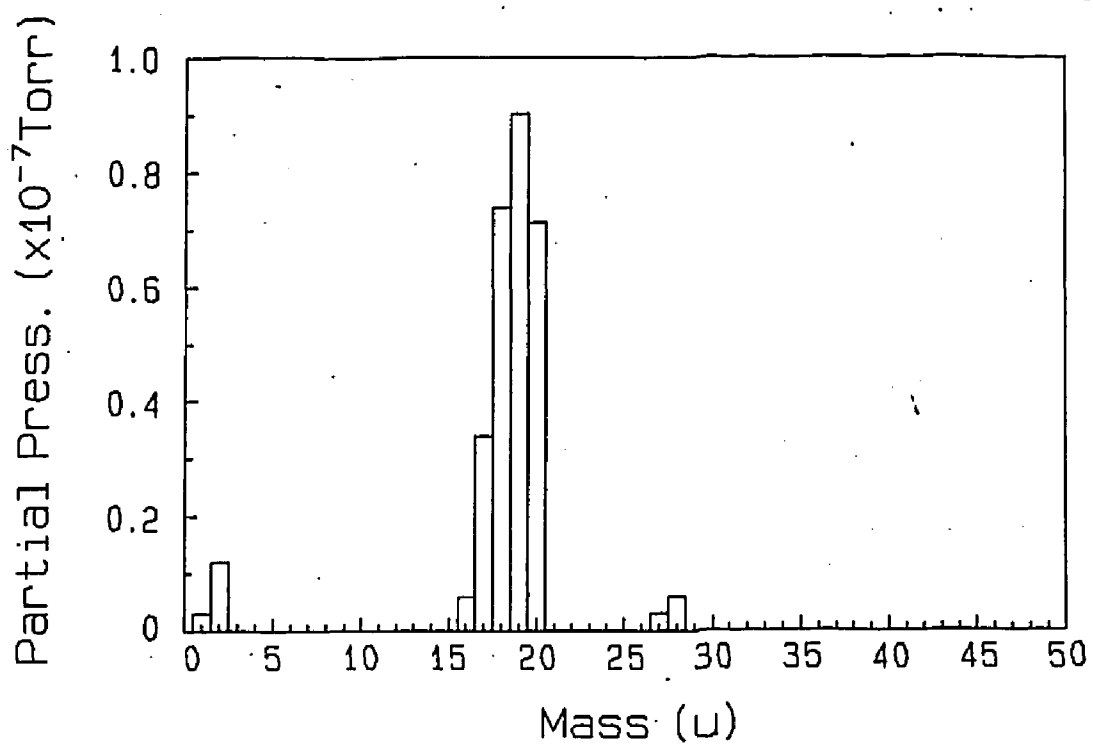


Fig. 2.29. Mass scan taken with the residual gas analyzer (Ametek model #M200) for D₂O gas exposure.

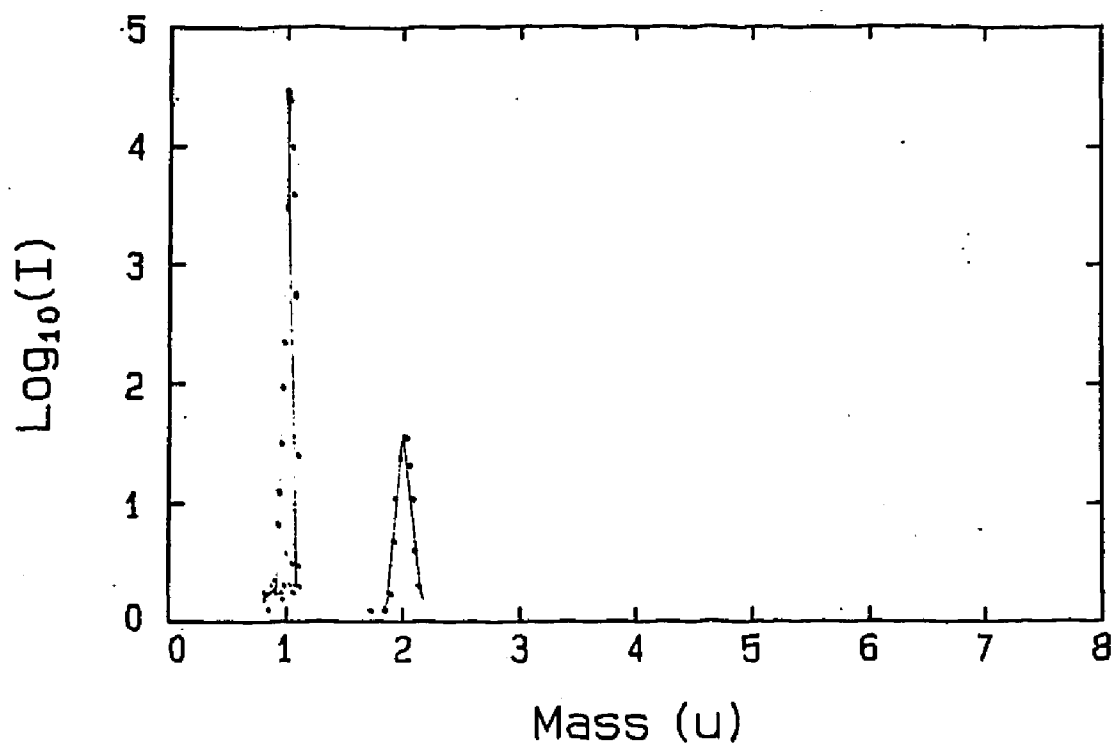


Fig. 2.30. Mass spectrum of negative ions sputtered by 100-eV K^+ impacting D_2O covered alkalated Mo.

signal. Experiments conducted with similar doses of D_2 did not result in any D^- signal. These results are again consistent with the oxide argument, which would say that hydrogen (or deuterium) cannot be injected into molybdenum at low energy because an oxide layer will also inhibit migration from vacuum into the surface. Clearly many more interesting experiments could be done to test these ideas by manipulating the oxide layer with various thermal cycles and controlling gas doses.

In summary, two facts indicate that O^- and O_2^- peaks in the spectra are due to an oxide layer on the Mo: (1), experiments conducted with doses of water showed that water had no effect on these secondary signals, and (2) heating the Mo to 1000 K did not eliminate the O^- or O_2^- signal. On the other hand, the yields of C_2^- and CH^- were observed to diminish upon heating, suggesting that these ions may have been due to trace amounts of hydrocarbon contamination ($<10^{-10}$ Torr) in the vacuum which adsorbed to the oxide layer.

D. Summary

Total negative ion and electron yields for collisions of positive alkali ions with a gas-covered, heterogeneous Mo surface have been measured. Mass analysis of the sputtered negative ions show that O_2^- is the dominant ion at low impact energies. This coupled with the fact that threshold energies are similar for secondary negative ions and electrons suggests that electron production is correlated to the O_2^- production, and specifically that electrons are the result of autodetachment of excited O_2^- and perhaps of other short-lived excited negative ions. It is shown that the work function plays a major role in determining both the negative ion and electron yields. The results are compatible with the electron-tunneling model of Yu³⁸. Investigations as to the source of the H^- were conducted. It was shown that water vapor is not an important direct source of any of the desorbed ions. Further evidence suggests that the source of the two oxygen negative ions (O^- , O_2^-) is the oxide layer on the Mo.

Future work should include detailed in situ investigations of the surface's composition and its relation to the sputtering of negative ions. Manipulation of the oxide layer could be done through the use of 1800 K bakeouts and careful O_2 doses.

CHAPTER 3
PHOTON-ASSISTED NEGATIVE ION
DESORPTION FROM LOW WORK FUNCTION SURFACES

A. Background

Photo-desorption of H^- from a barium substrate has been investigated for photons with wavelengths ranging from 245 to 585 nm. The principal aim of this work has been to examine the role of these photons in producing H^- at these low work function surfaces. The results of this chapter could be of interest to those who work with high current negative ion sources. It may be the case that photon-assisted negative ion desorption plays an important role in determining the concentration of H^- in these ion sources.

Interactions between photons and surfaces have been studied extensively.⁴⁵⁻⁴⁸ In addition to the surface analysis techniques which employ photons that were mentioned in the introduction to this thesis, much work has been done in studying the physics of photon interactions with adsorbate/surface interfaces. One particularly relevant application of photons with these interfaces is in the area of photon-assisted etching of electronic materials^{49,50}. Included in the adsorbate/surface work, extensive studies of

photochemistry at adsorbate/semiconductor interfaces have been conducted. Many of these experiments have concentrated on the conversion of solar energy to chemical energy.

This chapter will look at the interaction between photons and an adsorbate/metal system. Closely related to this field is the work done in the area of desorption induced by electronic transitions (DIET)⁵¹. There are two subfields within DIET studies that are very relevant to surface photochemistry; these are electron stimulated desorption (ESD)⁵¹ and photon stimulated desorption (PSD)⁵¹. These subfields include work directed at understanding the physics of neutral atom or ion (usually positive) desorption due to electron or photon impact. The same excitation pathways are relevant for both surface photochemistry and DIET processes⁴⁸.

The question now arises as to how a photon incident on an adsorbate/metal system can cause desorption of atoms in a PSD event. One of the commonly discussed mechanisms for PSD is the Menzel-Gomer-Redhead (MGR) or Franck-Condon-excitation mechanism⁵². In the MGR model, an electron from the bonding orbital between the desorbate species and the rest of the system is suddenly excited into an anti-bonding state. As a result of this Franck-Condon excitation (a molecular excitation in which the internuclear separation remains essentially unaltered while the electronic transition takes place), the desorbate species finds itself

on a repulsive potential curve and thus moves away from the surface⁵³.

For the present experiments, photon-driven reactions are treated not in the usual context of photon-adsorbate-metal surface systems in which the adsorbate is an impediment to energy transfer to the substrate, but with the notion that the barium sample used in these experiments is laced with interstitial hydrogen.

The desorption of surface species as a result of photon bombardment can arise from several different mechanisms⁵². These may be categorized as direct heating of the surface by photon bombardment, indirect, or resonant heating associated with resonant absorption of photons to produce vibrational excitation of adsorbed species. Also, there are the direct photon-stimulated processes mentioned before, where the excitation process leads directly to the desorption of an atom or molecule.

When studies using high energy, high intensity photon sources were first begun, it was hoped that surface analogies to gas-phase photochemistry could be developed. The problem is, however, that a molecule close to a solid surface has many pathways by which the excitation generated by photon absorption can be rapidly dissipated into the bulk of the solid. This occurs, for example, by phonon or plasmon excitation or by the generation of electron-hole pairs within the solid. In a few studies, true

photodesorption arising from vibrational excitation has been observed, but these studies usually involve systems in which an inert "spacer" layer (for example, an adsorbed inert gas) has been used to impede energy transfer from the excited adsorbed species to the substrate.

A large fraction of the photodesorption experiments can be explained in terms of the indirect, or resonant, heating mechanism⁵⁴. In this case, the initiating event is resonant photon absorption via a vibrational mode of an adsorbed molecule. Because the cross section for this process depends upon matching the photon energy to the vibrational mode frequency, the process shows the strong photon frequency dependence typical of gas-phase photochemical processes. However, because of the rapid redistribution of the energy of the initial excitation into the phonon modes of the substrate, the desorption events that follow the initial excitation are essentially thermal desorption events driven by local heating. It is important then to address the issue of thermal desorption when analyzing the results of the experiments to be presented in this chapter.

Now let us turn our attention to the barium surface which will be used in all of the photodesorption experiments presented here. The use of barium in negative hydrogen ion sources has been investigated extensively over the past several years²¹. These experiments have been motivated by the desire to construct a high current, high energy neutral

(H or D) beam injector to be used in nuclear fusion programs. Such a neutral beam can be produced by stripping the electrons from a high current, high energy H^+ beam. Van Os²¹ describes "surface conversion" which is one method of producing such high current H^+ beams. In this method, a converter surface is placed in contact with a hydrogen plasma; Fig. 3.1 shows a diagram of one of these hydrogen sources. Protons from the plasma strike the surface and most of these protons are implanted while some are scattered. Implanted hydrogen can come to the surface via diffusion or via removal of substrate material by sputtering. Surface hydrogen atoms are sputtered by the incident flux and a fraction of the sputtered and scattered particles will form H^+ via resonant charge exchange with the converter surface.

Resonant charge exchange from a metal surface to an atom can occur as a result of electron tunneling between the electronic states at the surface and the valence states of the hydrogen. When a hydrogen atom is near a metal surface, the electron affinity level of the atom shifts to lower energy due to the interaction of the atom with its image charge in the metal. As the atom approaches the metal surface, a distance is reached where the affinity level of the atom crosses the work function of the metal, but is broadened due to this interaction. Subsequently, an electron from the metal can tunnel between the conduction

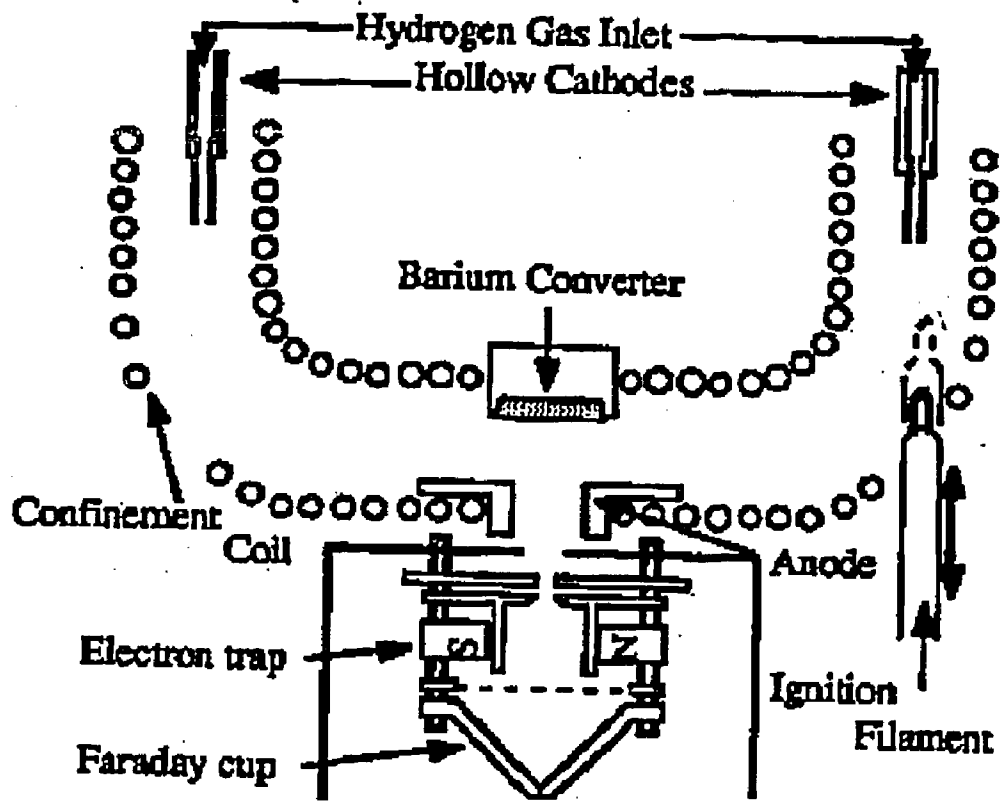


Fig. 3.1. Experimental set-up of the Amsterdam Light Ion Conversion Experiment, ALICE.

band and the affinity level of the atom. In Gadzuk's theory of resonant charge exchange⁹, it is shown that the transition rate is strongly dependent on the Fermi energy, i.e. the width of the conduction band of the metal.

The paramount observation of the experiments to be presented here is that photodesorption of H^- from a barium converter substrate does occur with a yield increasing almost exponentially with photon energy. A plausible mechanism for the production of H^- will be discussed, and comments on the consequences to the "surface conversion" experiments described above will be given.

B. Experimental Apparatus and Methods

A schematic diagram of the apparatus used in the studies presented here is shown in Fig. 3.2. Photons from an optical delivery system are focused into the vacuum chamber and onto the barium sample. Negative ions which leave the barium sample are focused into a 90° electrostatic beam bender. The ions then enter another lens stack where they are focused into the aperture of the magnetic mass analyzer described in Chapter 2 and are subsequently detected by the particle multiplier. As before, the ions pass through the spectrometer tube with fixed kinetic energy and, if desired, a mass spectrum can be obtained by varying the magnetic field. The experiment is conducted in the same vacuum system used in the negative ion and electron emission surface experiments.

The electrostatic beam bender includes two concentric plates spaced $\frac{1}{4}$ " apart, having radii r_1, r_2 of 2" and $2\frac{1}{4}$ " respectively. The ions enter the beam bender with energy ϵ (eV). The beam bender passes the ion beam when the voltage between the two plates ΔV is :

$$\Delta V = 2e \ln\left(\frac{r_2}{r_1}\right), \quad (3.1)$$

which gives

$$\Delta V = .637e \quad (3.2)$$

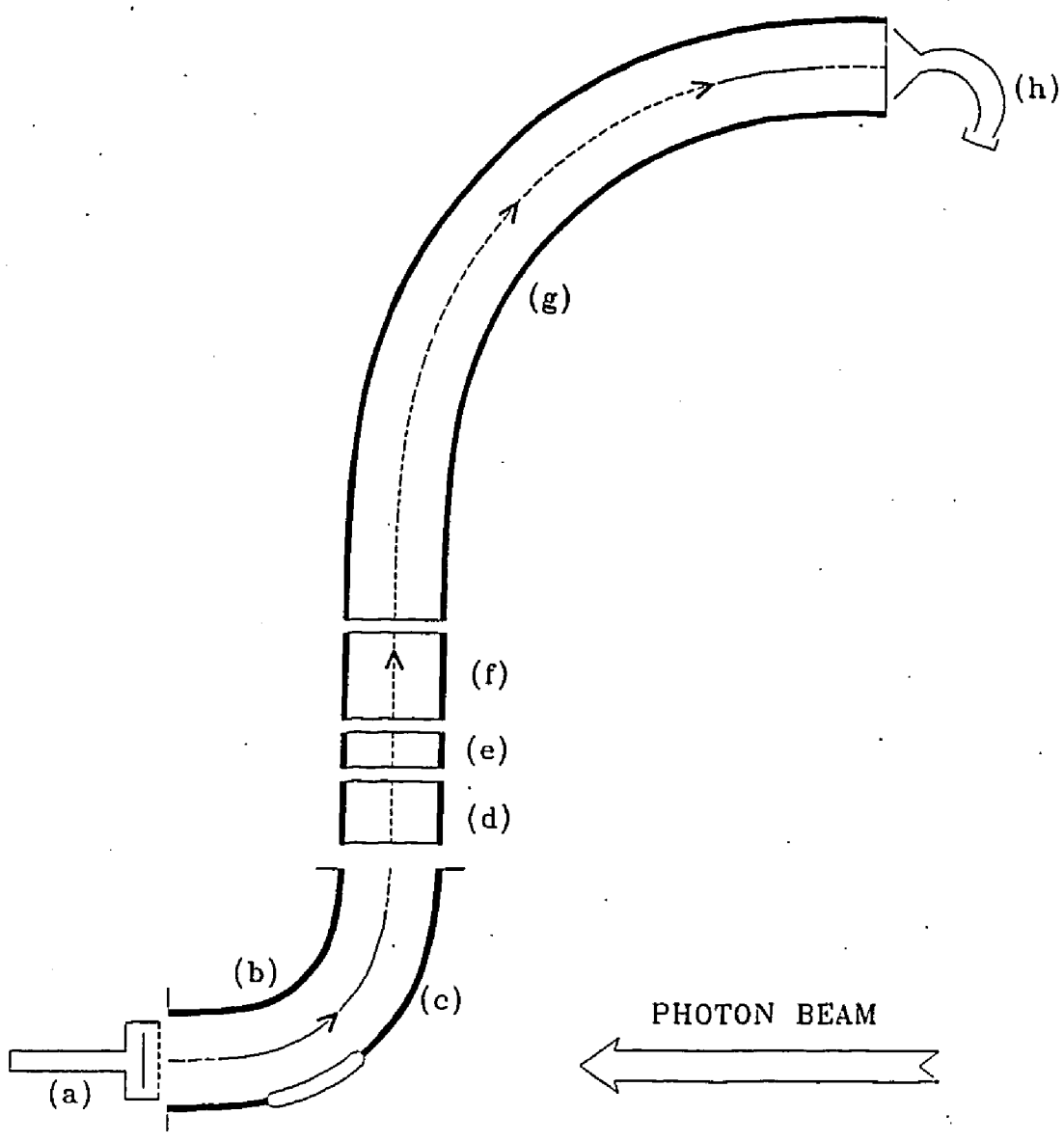


Fig. 3.2 Schematic diagram of experimental apparatus. (a) Ba surface; (b) and (c) beam bender; (d), (e), and (f) lens; (g) magnetic momentum analyzer; (h) particle detector.

for the design parameters stated above.

All surfaces in the vicinity of the barium sample are biased with respect to the mass spectrometer such that the negative ions formed on surfaces other than the barium cannot reach the detector.

Fig. 3.3 shows a schematic of the optical system. Photons of various wavelengths are focused onto the barium sample in the following manner. A 1 kW Hg vapor arc lamp (Oriel #6287) serves as the source for the photon beam. The optical beam is passed through a water IR filter (Oriel #6123) which contains an outer water jacket through which water flows to cool the filter. The photon beam is then focused into the slit of a monochromator (Oriel #77200). The monochromator contains a 1200 line/mm grating and is capable of 0.1 nm resolution with proper choice of slits. The selected wavelength is then focused through a UV-transparent sapphire window mounted on a vacuum flange. The beam then passes through an aperture in the outer cylindrical element of the electrostatic beam bender and subsequently strikes the Barium surface.

The absolute intensity of the photon beam is determined in situ by replacing the barium sample with a calibrated photodiode (Oriel #7181). The spectrum measured with this configuration is shown in Fig. 3.4. The photo-diode calibration was checked using a photometer borrowed from NASA-Langley Research Center.

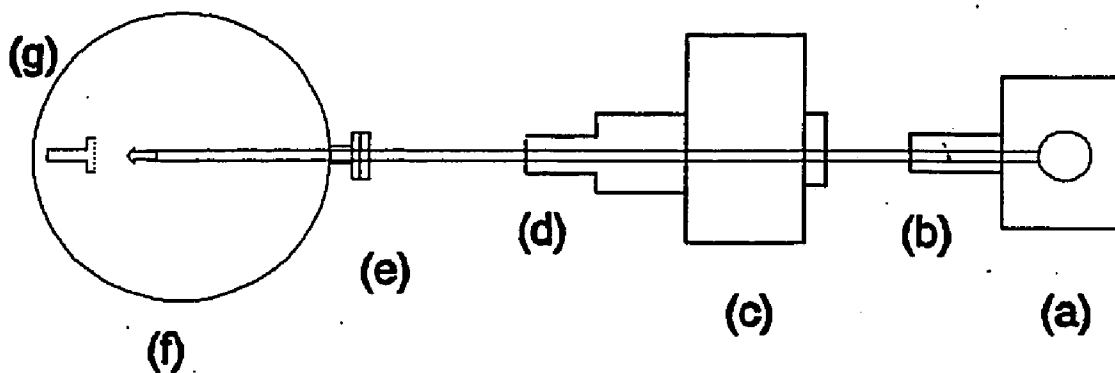


Fig. 3.3. Schematic diagram of optical delivery system. (a) Hg lamp housing; (b) IR filter; (c) monochromator; (d) lens; (e) quartz window; (f) vacuum chamber; (g) barium.

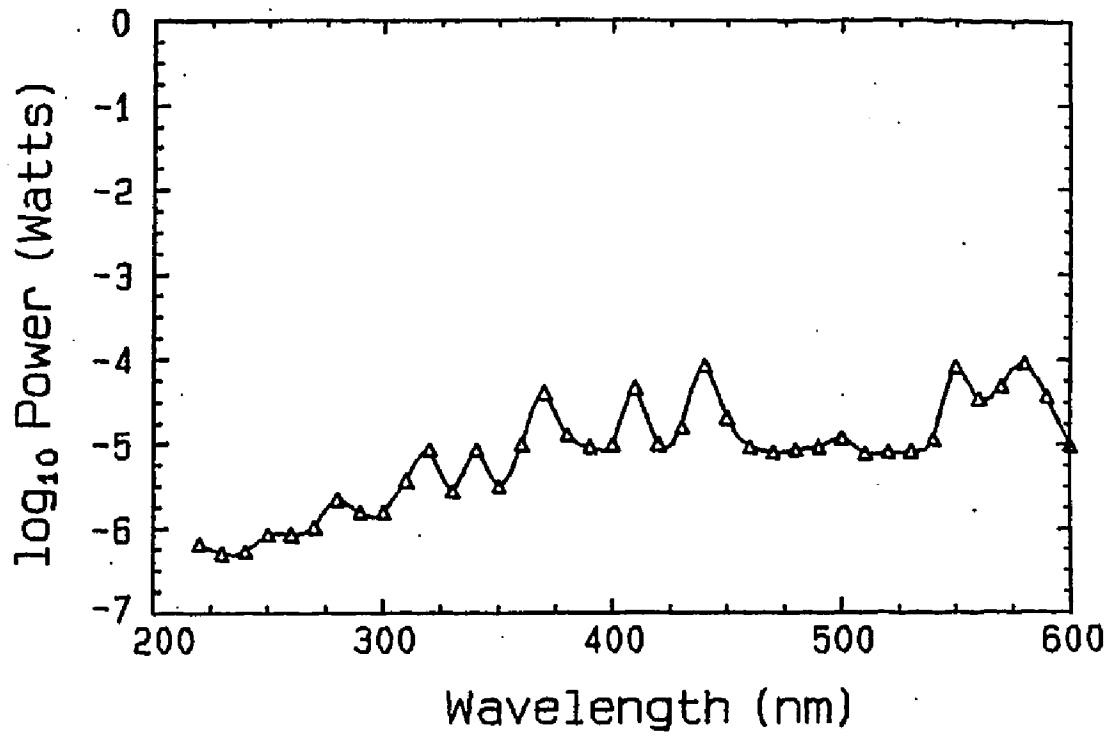


Fig. 3.4. Spectral power of Hg lamp.

The barium was obtained from the Notre Dame Radiation Lab in a housing such that it can be used as a thermionic electron source. The barium surface is in contact with a Nichrome heater wire which is inside the barium, and a Tungsten extraction grid is placed in front of the barium surface.

In order to condition the barium, the sample is maintained at a temperature of 1000 °C for approximately one half-hour. This conditioning period is necessary in order to obtain stable electron emission current (10-30 μ A). It is believed that the role of the conditioning procedure is to purge the barium surface of impurities, and hence lower its work function. Immediately before photodesorption experiments were conducted, the barium was conditioned as described above and then allowed to cool to a temperature of 200°C, for a period of about 15 minutes.

C. Results and Discussion

The relative yield of photodesorbed H^- , i.e. the number of negative hydrogen ions desorbed per incident photon is shown in Fig. 3.5 as a function of photon energy. The number of photons striking the surface is the measured power (taken from Fig. 3.4) divided by the photon's energy. For the results of Fig. 3.5, the barium sample was heated to 1000 °C to obtain stable electron emission for approximately 1/2 hour and then allowed to cool for a period of about 10 minutes. The yield of H^- was then measured for various wavelengths.

The H^- yield, as seen in Fig. 3.5, exhibits a very strong dependence on the incident photon energy, with higher energy photons giving rise to a higher yield of photo-desorbed H^- . A threshold energy for the production of H^- is clearly observed in the vicinity of 3 eV. This is observed to be the case for all sets of data collected.

As was mentioned in the introduction of this chapter, many photodesorption experiments can be explained in terms of a heating mechanism. Two experiments were designed to investigate the possibility that the observed H^- ions were due solely to the heating of the surface by the photon beam.

The first of these experiments consisted of replacing the optical delivery system (Hg lamp and monochromator) with a Nd:YAG laser. This laser (Quantronix model #331) operates

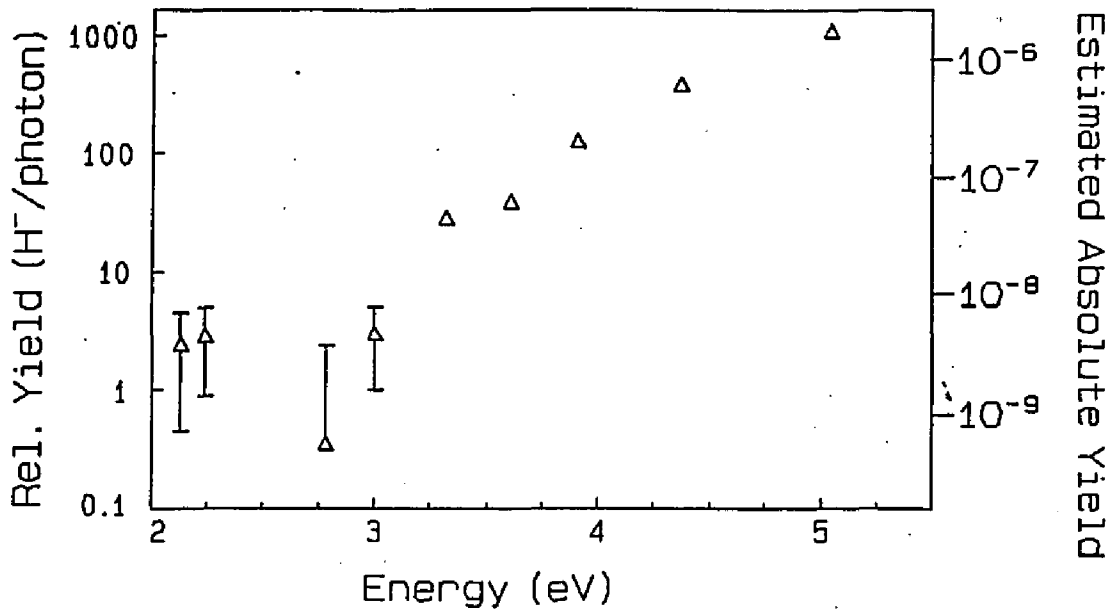


Fig. 3.5. Yield of H⁻ as a function of photon energy. An estimate of the absolute scale is provided.

at a wavelength of 1064 nm and, in the pulsed mode, delivers 2 mJ during a 1 μ sec period at a repetition rate of 100 Hz. Despite the 2 kW of instantaneous power, and 0.2 W of average power, no negative ions were observed due to heating. One might make the argument that metals strongly reflect the 1064 nm photons, however some fraction of the photons in this wavelength region will be absorbed by the barium. The incident power from the Nd:YAG upon the surface is some six orders of magnitude greater than that of the Hg lamp used to acquire the data shown in Fig. 3.5.

In the second experiment to investigate the possibility of thermal desorption, the surface was exposed to a large dose of carbon tetrachloride vapor (CCl_4). It is known that Cl^- is easily produced by exposing a hot metal surface to CCl_4 . Using the gas handling system describe in Chapter 2, the pressure in the vacuum chamber was maintained at 10^{-6} Torr of CCl_4 for 10 minutes (6 Langmuir). After this dosing, the barium was then heated to 1000°C .

Fig. 3.6 shows a mass scan of the negative ions thermally desorbed from the barium sample at 1000°C . A large Cl^- peak is observed. H^- is also present in the mass spectrum but at an intensity nearly three orders of magnitude less than that of Cl^- .

After cooling the Ba sample to 200°C , photodesorption data was collected in the manner described at the beginning of this section. This data is identical to that shown in

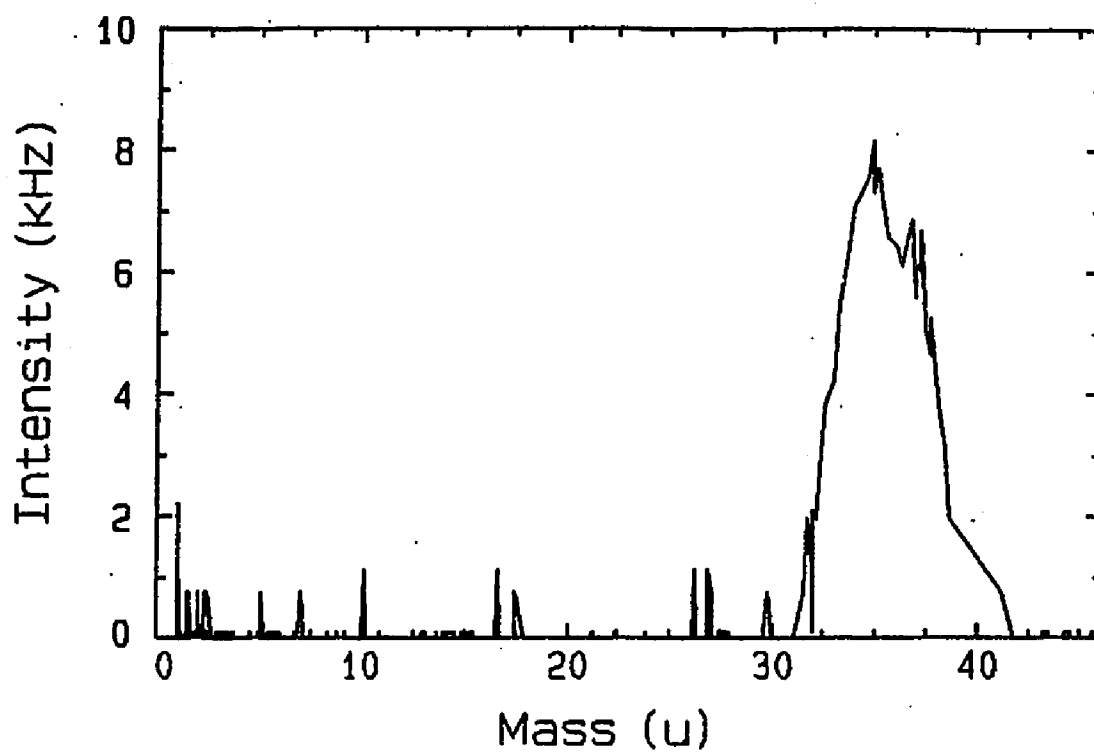


Fig. 3.6. Mass spectrum of negative ions desorbed while heating Ba sample.

Fig. 3.5. In addition, no Cl^- peak was observed at any of the wavelengths of the Hg lamp! Finally it should be noted that H^- yields do not increase during illumination as one might expect in a thermal desorption experiment.

These two experiments clearly demonstrate that the mechanism for producing H^- from the Ba sample using UV - visible photons is not a thermal mechanism. In addition, the results of Fig. 3.5 are consistent with this inference since the data in Fig. 3.5 are normalized to the photon beam power.

This then leads to the question of just how the H^- production occurs. As was mentioned in the introduction to this chapter, photon-stimulated processes leading to direct desorption of an atom or a molecule are known to occur. In the case of the Ba-H system, van Os has measured the surface binding energy of hydrogen to barium and found it to be 1.2 eV ²¹, implying that an incident photon with energy greater than 1.2 eV could photo-desorb a hydrogen atom from the barium surface. The resulting situation, neutral hydrogen leaving a low work function barium surface, is identical to that of the experiments described by Van Os.²¹ Resonant electron transfer which would form H^- can then take place provided the ejected hydrogen atom has a sufficient component of velocity perpendicular to the barium surface. Fig. 3.7 shows data for the electron attachment probability as measured by Los and Geerlings¹⁷ for hydrogen leaving a

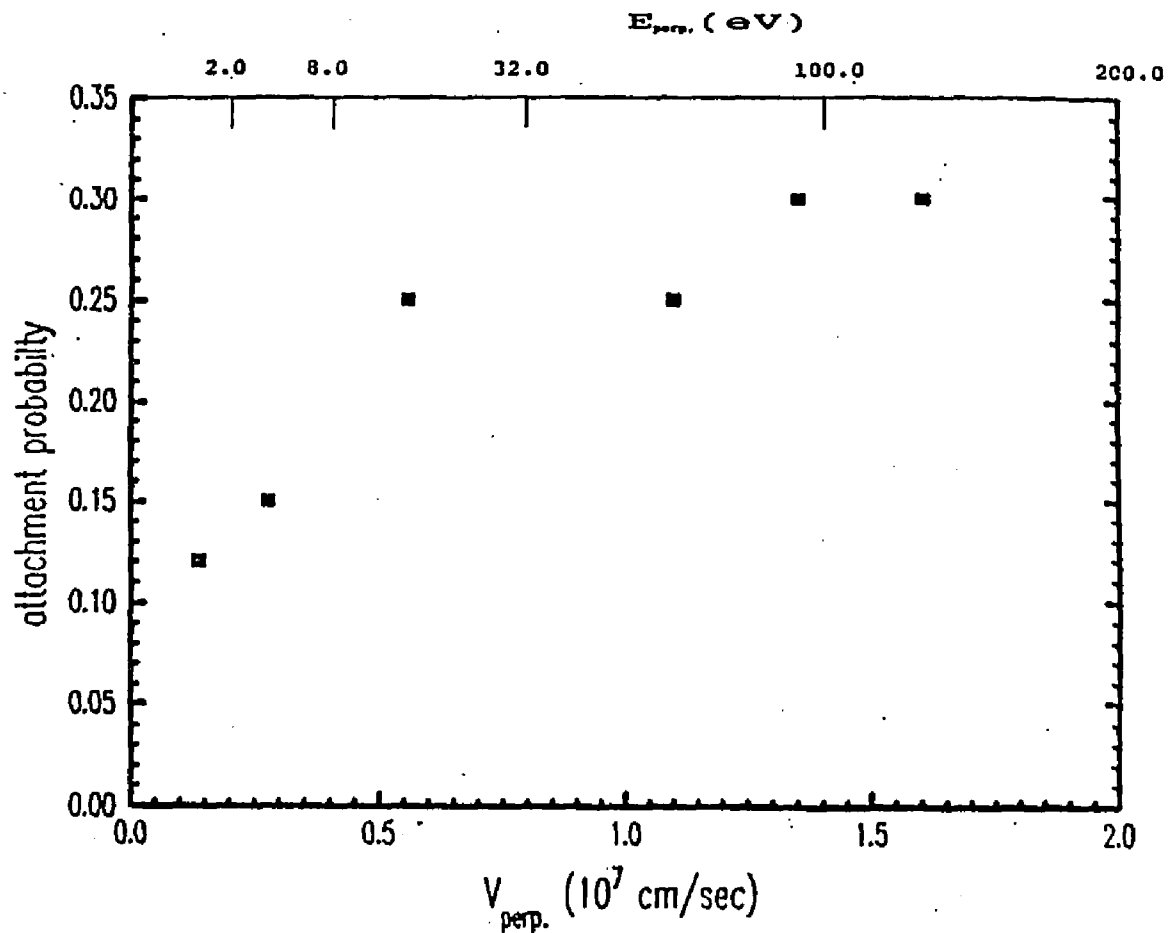


Fig. 3.7. Attachment probability for the formation of H^- vs. asymptotic normal velocity or normal energy component.

barium surface as a function of outgoing velocity normal to the barium surface and the equivalent kinetic energy⁵⁵. Even at relatively low energies (~0.5 eV), there is still a significant probability of electron attachment.

Now let us turn our attention to the energetics of this process. Dissociating a bound surface hydrogen atom from barium requires 1.2 eV. The work function of barium is 2.5 eV. The energy released by the formation of H⁻ from H⁰ is .75 eV. This gives an energy threshold for photodesorbing H⁻ to be 1.2 eV + 2.5 eV - 0.75 eV = 3.0 eV. This result is close to the experimental result for the threshold energy obtained from Fig. 3.5.

It is of interest to estimate the absolute yield for this photodesorption process. The yield is defined simply as the number of H⁻ produced per incident photon,

$$Yield = \frac{H^- \text{ desorption rate}}{\text{photon impingement rate}}. \quad (3.3)$$

The flux of incident photons is the measured photon power at a given Hg line divided by that line's energy. For the case of 4.4 eV photons, Fig. 3.4 shows a measured power of 2 μ W, which is consistent with 3×10^{12} photons per second striking the photodiode. The intensity of the H⁻ beam detected during illumination with 280 nm (4.4 eV) photons was about 5/sec. The channeltron is operated in the pulse mode and the overall transmission efficiency of the mass spectrometer

has been estimated to be 0.1% and the transmission efficiency of the 90° electrostatic beam bender is estimated to be 1%. This puts the H⁻ desorption rate from the barium at:

$$\frac{5 \text{ ions}}{\text{sec}} (10^2) (10^3) = \frac{5 \times 10^5 \text{ ions}}{\text{sec}}$$

This leads to an absolute yield of approximately 10⁻⁷/photon at a wavelength of 280 nm. It should be emphasized that we know nothing about the concentration of Hydrogen in this Barium sample.

Using the estimate for the absolute yield and extrapolating the curve in Fig. 3.5 to energies comparable to Lyman- α lines in the hydrogen spectrum, it becomes apparent that the photons produced in hydrogen plasmas could be another source of H⁻ previously overlooked. Fig. 3.8 shows this extrapolation and it is apparent that a substantial yield of H⁻ might result from the impact of photons with energies comparable to Lyman- α on barium surfaces. This result could have implications regarding the production of H⁻ using proton bombardment generated from discharges.

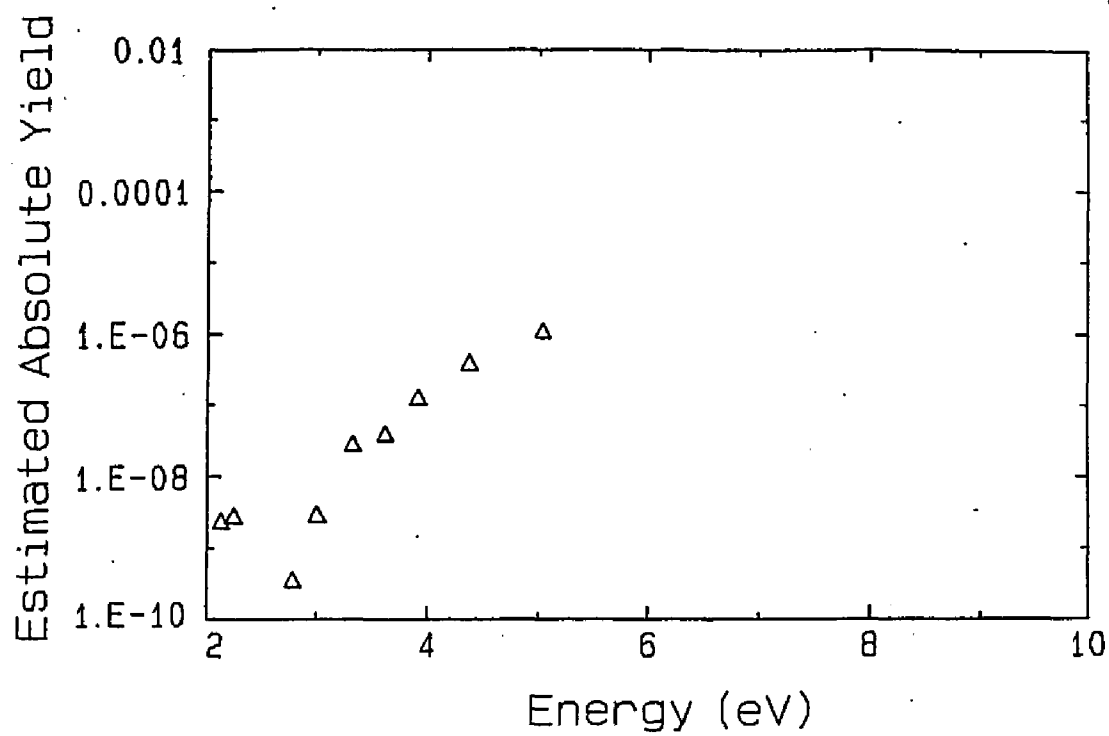


Fig. 3.8. Estimated absolute yield of H^- as a function of photon energy; the ordinate is extended to energies comparable to Lyman- α photons.

D. Summary

Relative yields for photo-desorbed H^- from a barium substrate have been measured as a function of photon wavelength for the range of 245 to 585 nm. It has been demonstrated that thermal desorption is not the mechanism responsible for observed H^- . A model for the formation of negative ions due to photons impinging on a low work function surface has been presented. Based on a simple model, the energetics of the suggested ion emission process predict a threshold energy around 3 eV; the experimental results are in good agreement with this value. An estimate of the absolute yield of photo-desorbed H^- per incident photon has been made.

Obviously, it would be of great interest to measure absolute H^- yields at higher photon energies, for example in the range from 5 eV to about 10 eV (Lyman- α). Future work should include an investigation into the source of hydrogen in barium, and improvements in the optical delivery system must be made. These improvements could involve a UV laser or perhaps the experiment could be taken to a synchrotron light source.

CHAPTER 4

CONCLUSION

The experiments discussed in this thesis were designed to investigate the secondary negative products emitted from metal surfaces due to the collision of low energy particles.

In Chapter 2, the experiments dealing with electron and negative ion emission from gas covered surfaces due to the impact of low energy positive alkali ions were discussed. Absolute yield measurements as a function of impact energy for the electrons and the negative ions were performed. It was observed that the threshold energies for the production of electrons and negative ions were similar. In addition to these yield measurements, mass analysis of the secondary negative ions was performed. It was demonstrated that near the energetic threshold, the negative ion signal consisted primarily of O_2^- . It was then suggested that collisionally-formed autodetaching O_2^- was the principal source of electrons in the near-threshold region. This suggestion could explain the origin of electrons due to low energy ions impacting gas covered surfaces. The model for electron emission presented herein is consistent with previous work which observed that electron yields are strongly dependent on surface conditions.

Further testing of the hypothesis that emitted electrons are due to O_2^- (and thus from the metal's oxide layer) must include careful manipulation and monitoring of the metal's oxide layer. Removal of the oxide layer could be done in various ways (e.g. 1800 K bakeout of the surface as described by M.L. Yu, in situ cleaving, Ar^+ bombardment, or localized He glow discharge). The easiest of these techniques to implement would be the He glow discharge. Once a clean (i.e. oxide-free) metal surface was produced, an oxide layer could be formed in a controlled manner using careful doses of O_2 .

While all of the experiments in Chapter 2 were performed on a Mo surface, it is of great interest now to characterize Nb. The interest in Nb stems from its use in the superconducting radio frequency accelerator cavities at the Continuous Electron Beam Accelerator Facility and elsewhere. In addition to the measurements of electron and negative ion yields, the Nb studies should include investigations of the diffusion of H in Nb. It is thought that the hydrogen content in the Nb cavities can affect their performance. As was mentioned in the background section of Chapter 2, SIMS experiments are the most useful when detection of hydrogen is of interest.

In Chapter 3, experiments dealing with the photodesorption of negative ions from low work function surfaces were discussed. It was shown that non-thermal

photodesorption of H^- from a barium substrate due to photons does occur in the photon energy range from 3 eV to 5 eV.

An intuitive model based on a Franck-Condon mechanism was presented. The photon threshold energy observed is consistent with this model. An estimate of 10^{-7} /photon for the absolute yield of photo-desorbed H^- has been made for photons with a wavelength of 280 nm (4.4 eV).

Future photodesorption experiments must employ a different light source. The Hg lamp's few UV lines give rise to only a qualitative description of the relative yield of H^- as a function of photon energy. The possibility of transporting the experiment to the CAMD (Center for Advanced Microstructure Devices) Synchrotron at Louisiana State University does exist. This would be an excellent light source for conducting these experiments for a number of reasons. First, a continuous spectra of UV photons would be available. Second, the intensity of the radiation from the synchrotron is greater than that from the Hg lamp. Finally, photons comparable to Lyman- α energies would be available. It will be interesting to measure the absolute yield of photodesorbed H^- at these energies.

As a final thought, the author would like to make the following comments concerning surface physics. Applying science to solve some of physics' topical questions has led to the construction of fusion devices, accelerators, synchrotrons, etc.. These devices are not built out of

well-characterized single crystal materials. Rather they are constructed with various stainless steels, aluminum, niobium, and so forth. The materials just listed intrinsically may contain oxides, carbides, interstitial hydrogen, water, grain boundaries, etc.. The effects of the properties listed, specifically the physics of these material's surfaces lead to problems (and opportunities) which must be understood when considering the construction and operation of the projects just mentioned. This is an exciting time to be involved in the field of surface physics as work is being done to understand these so-called "technical" surfaces and their role in various large scale projects.

References

1. W. R. Grove, *Philos. Mag.* 5, 203 (1853).
2. J.P. Gassiot: *Philos. Trans. Roy. Soc. London* 148, 1 (1958).
3. E. Golstein, *Verh. Dtsch. Phys. Ges.*, 4, 228 (1902).
4. J. Stark, *Z. Elektrochem.* 14, 752 (1908); 15, 509 (1909).
5. F. L. Arnat and J. C. Milligan, *Proc. Roy. Soc. Ser. A*, 156 (1936) 538.
6. R. H. Sloane and R. Press, *Proc. Roy. Soc. Ser. A*, 168 (1938) 284.
7. V. I. Veksler and M.B. Ben'iaminovich, *Sov. Phys. Tech. Phys.*, 1 (1957) 1626.
8. R. E. Honig, *J. Appl. Phys.*, 29 (1958) 549.
9. J. A. McHugh, *Secondary Ion Mass Spec.*, Chap. 6 in Methods of Surface Analysis, A. W. Czanderna, ed.
10. Dunaev, Yu.A., and I.P. Flaks: *Secondary Emission Induced by Bombarding the Metal Target with Multicharge Ions. Doklady Akad. Nauk* 91, No.1, 43 (1953).
11. *Emission of Electrons and Reflection of Ions from Metal Surfaces. Doklady Akad. Nauk S.S.S.R.*, 79, 775 (1951).
12. *Ion-Electron Emission as a Function of Certain Parameters of the Target and the Bombarding Ions. Akad. Nauk S.S.S.R., Bull., Physic. Ser.* 24, 666 (1960).
13. D. Lichtman, *A Comparisons of the Methods of Surface Analysis and their Applications*, Chap. 2 in Methods of Surface Analysis, A. W. Czanderna, ed.
14. X.-L. Zhou, X.-Y. Zhu and J. M. White, *Surf. Sci. Reports* 13, (1991) pg. 73.
15. J. K. Norskov and B. I. Lundqvist, *Phys. Rev. B* 19 5661 (1979).
16. R. Brako and D. M. Newns, *Surf. Sci.* 108, 253 (1981).

17. J. Los and J. J. C. Geerlings, Charge Exchange in Atom-Surface Collisions, Physics Reports 190, No. 3 (1990) 133-190.
18. R. Gomer and L.W. Swanson, J. Chem. Phys., 38 (1963) 1613.
19. J. W. Gadzuk, Surf. Sci. 6 (1967) 133, 6 (1967) 159.
20. P. W. Van Amersfoort, Formation of Negative Ions on a Metal Surface.
21. Ron van Os, Negative Ion Sourcery, 1989.
22. H. D. Hagstrum, Phys. Rev. 96, 325 (1954) 96, 336 (1954).
23. D. W. Vance, Phys. Rev. 169, 263 (1968).
24. J. Ferron, E. V. Alonso, R. A. Baragiola, and A. Oliva-Floria, J. Phys. D 14 1707 (1981).
25. H. Brenten, H. Muller, and V. Kempter, Z. Phys. D 21, 11 (1990).
26. G. Lakits, F. Aumayr, M. Heim, and H. Winter, Phys. Rev. A 42 5780 (1990).
27. H. Winter, F. Aumayr, and G. Lakits, Nucl. Instrum. Methods Phys. Res. Sect. B 58, 301 (1991).
28. J.A. Ray et al., J. Appl. Phys. 50, 6516, (1979).
29. M. Kaminsky, Atomic and Ionic Impact Phenomena on Metal Surfaces (academic, New York, 1965), p. 263ff.
30. E.V. Alonso et al., Phys. Rev. B22, 80 (1980).
31. A. Zangwill, Physics at Surfaces (Cambridge University Press, Cambridge, England, 1989), p. 173.
32. J. C. Vickerman, in Methods of Surface Analysis: Techniques and Applications, edited by J. M. Walls (Cambridge University Press, Cambridge, England, 1989), p. 173.
33. R.A. Langley et al., Data Compendium for Plasma Surface Interactions (International Atomic Energy Agency, Vienna, 1984), p.104.
34. Spectra-Mat Corp. Watsonville, CA 95077.

35. J. Moore et al., Building Scientific Apparatus (Addison Wessley, London, 1983), p.308.
36. D. Scott, M. S. Huq, R. L. Champion, and L. D. Doverspike, Phys. Rev. A 32, 144 (1985).
37. Galileo Electro-Optics Corp., Galileo Park, Sturbridge, MA 01518.
38. M. L. Yu, Phys. Rev. Lett. 40, 574 (1978).
39. F. Reif, Fundamentals of Statistical and Thermal Physics (McGraw Hill, New York, 1965), p. 273.
40. M. L. Yu, Charged and excited States of Sputtered Atoms in Sputtering by Particle Bombardment III ed. by R. Behrisch and K. Wittmaack, Springer-Verlag, New York, (1991).
41. I. S. T. Tsong, N. A. Yusuf, Appl. Phys. Lett. 33, 999 (1978).
42. H. P. Bonzel, Surf. Sci. Rep. 8, 43 (1988).
43. M. L. Yu, Phys. Rev. Lett. 47, 1325 (1981).
44. G. Moraw, R. Dobrozemsky, Proc. 6th Intl. Vac. Cong. 1974, Jap. J. Appl. Phys. Suppl 2, Pt. 1, 1974, pg. 261
45. D. Lichtman, A. Comparison of the Methods of Surface Analysis and their Applications, in Methods of Surface Analysis, ed. Czanderna pg. 58, Elsevier, New York, 1975.
46. M. Anpo, T. Matsuora, eds. Photochemistry on Solid Surfaces. Amsterdam, Elsevier, 1989.
47. T. J. Chuang, Laser-induced gas-surface interactions. Surface Sci. Reports 1983, 3:1.
48. X.-L. Zhou, X.-Y. Zhu, J. M. White, Photochemistry at Adsorbate/Metal Interfaces.
49. F. A. Houle, Phys. Rev. Lett. 61, no. 16, pg. 1871 (1988).
50. D. J. Ehrlich, J. Y. Tsao, J. Vac. Sci. Tech. B1 (1983) 969.

51. DIET I, Eds. N.H. Tolk et al. (Springer, Berlin, 1983);
DIET II, Eds. W. Brenig et al. (Springer, Berlin, 1985);
DIET III, Eds. R. Stulen et al. (Springer, Berlin, 1988);
DIET IV, Eds. G. Betz et al. (Springer, Berlin, 1990).
52. R. A. Rosenberg et. al., Photon Stimulated Ion Desorption
from Condensed Molecules: N_2 , CO, C_2H_2 , CH_3OH , N_2O , D_2O ,
and NH_3 , in DIET I ed. by N. H. Tolk et. al., Springer
Verlag, New York (1983) pg. 247.
53. P. J. Feibelman, Mechanisms of "Electronic" Desorption,
in DIET I ed. by N. H. Tolk et. al., Springer Verlag, New
York (1983) pg. 61.
54. J. Hudson, in Surface Science, (Butterworth-Heinemann,
Boston, 1991).
55. C.F.A. van Os et al., Proc III European Workshop on the
Production and Application of Light Negative Ions, p.266,
(Amersfoort, Netherlands, 1988).

Vita

Douglas H. Baker

Born on July 6, 1964 in Riverside, New Jersey.

He graduated from Elderton High School in 1982. He received his B.S. degree in physics from Indiana University of Pennsylvania in 1986. He received his M.S. degree in physics from the College of William and Mary in Virginia in 1988.